



# Rare earth element cycling in the pore waters of the Bering Sea Slope (IODP Exp. 323)



Tseren-Ochir Soyol-Erdene<sup>a,1</sup>, Youngsook Huh<sup>a,b,\*</sup>

<sup>a</sup> School of Earth and Environmental Sciences, Seoul National University, Seoul 151-747, Republic of Korea

<sup>b</sup> Research Institute of Oceanography, Seoul National University, Seoul 151-747, Republic of Korea

## ARTICLE INFO

### Article history:

Received 18 April 2013

Received in revised form 27 August 2013

Accepted 27 August 2013

Available online 10 September 2013

Editor: U. Brand

### Keywords:

Integrated Ocean Drilling Program

JOIDES resolution

Expedition 323

Site U1345

Reaction rate

Flux

## ABSTRACT

We studied the diagenetic behavior of rare earth elements (REEs) in a highly productive passive margin setting of the Bering Sea Slope. Site U1345 was drilled during the Integrated Ocean Drilling Program Expedition 323 at a water depth of 1008 m currently in the center of an oxygen minimum zone. Pore water concentrations of fourteen REEs were determined down to ~140 meters below the seafloor (mbsf). The REE concentrations were higher in the pore water than the deep seawater, indicating that there was significant liberation from the sediments during diagenesis. There was a major peak at ~10 mbsf that was more pronounced for the heavy REE (HREE); this peak occurred below the sulfate-methane transition zone (6.3 mbsf) and coincided with high concentrations of dissolved iron and manganese. At ~2 mbsf, there was a minor peak in REE and Mn contents. Below ~40 mbsf, the REE concentration profiles remained constant. The Ce anomaly was insignificant and relatively constant (PAAS-normalized Ce/Ce\* =  $1.1 \pm 0.2$ ) throughout the depth profile, showing that the Ce depleted in seawater was restored in the pore water. HREE-enrichment was observed over the entire 140 m except for the upper ~1 m, where a middle REE (MREE)-bulge was apparent. REE release in shallow depths (2–4 mbsf) is attributed to the release of light REEs (LREEs) and MREEs during the organoclastic reduction of Mn oxides in anoxic sediments. The high HREE concentrations observed at ~10 mbsf can be attributed to the reduction of Fe and Mn minerals tied to anaerobic oxidation of methane or, less significantly, to ferromagnesian silicate mineral weathering. The upward diffusion flux across the sediment–water interface was between 3 (for Tm) and 290 (for Ce)  $\text{pmol m}^{-2} \text{y}^{-1}$ .

© 2013 Elsevier B.V. All rights reserved.

## 1. Introduction

Pore waters are sensitive to post-depositional processes in sediments, while the solid phase is less responsive. Increasing a dissolved constituent's concentration reflects the remineralization and dissolution of or desorption from organic and mineral matter, whereas depletion indicates different processes, such as mineral precipitation in situ and chemical adsorption. Therefore, the pore water composition may be used to quantify the reaction rates and resulting fluxes of chemical species. The rare earth elements (REEs; La to Lu) can be powerful markers for these post-depositional processes, because their chemical properties systematically vary across the series and cerium (Ce) is sensitive toward redox conditions. The REE composition of pore waters is useful for evaluating the flux across the sediment–water interface and for establishing the oceanic REE budget (Elderfield and Sholkovitz, 1987; Sholkovitz et al., 1989; Schacht et al., 2010).

The analytical challenges caused by the small sample volumes and relatively low concentrations ( $\text{pM} = 10^{-12} \text{ M}$  level) have hampered the study of REEs in pore waters. Previously, only the upper decimeters of sediment, including the oxic, manganoous and ferruginous zones (Canfield and Thamdrup, 2009), have been analyzed (Elderfield and Sholkovitz, 1987; Sholkovitz and Elderfield, 1988; German and Elderfield, 1989; Sholkovitz et al., 1989; Sholkovitz et al., 1992; Haley et al., 2004; Schacht et al., 2010; Bayon et al., 2011b); these studies determined that significant fractionation among the REEs occurs in the pore waters during both removal and production. In the upper few centimeters, REEs are released when Mn and Fe are reduced (Sholkovitz et al., 1989; Haley et al., 2004). Additionally, the diagenetic degradation of particulate organic carbon (POC) and volcanic ash layers may be substantial REE sources in the pore waters (Haley et al., 2004; Schacht et al., 2010). Uptake of REE from pore waters is poorly understood. Precipitation of phosphate-bearing minerals (e.g., fluorapatite), Fe oxides and barite are potential sinks for the REE in pore water (Haley et al., 2004; Schacht et al., 2010). Recently, Kim et al. (2012) investigated REEs in deeper pore waters (up to 300 mbsf) and observed the REE released during POC degradation in methanogenic zones.

The Bering Sea is the third largest marginal sea in the world and can be divided into a shallow continental shelf (<200 m water depth) and

\* Corresponding author at: School of Earth and Environmental Sciences, Seoul National University, Seoul 151-747, Republic of Korea. Tel.: +82 2 880 9167; fax: +82 2 871 8752.

E-mail address: [yuhuh@snu.ac.kr](mailto:yuhuh@snu.ac.kr) (Y. Huh).

<sup>1</sup> Present address: School of Chemistry and Chemical Engineering, National University of Mongolia, Ulaanbaatar 14201, Mongolia.

deep basins (>3500 m) (Fig. 1). The Integrated Ocean Drilling Program (IODP) Site U1345 is located on the highly productive Bering Sea Slope proximal to the gateway leading to the Arctic Ocean (Takahashi, 1999). The pore water samples from this site allow the REEs to be studied in a passive margin setting; the signals for the diagenetic processes are not affected by fault systems, unlike convergent margin settings.

We present 14 REEs' high depth-resolution measurements from pore waters down to ~140 meters below the seafloor (mbsf); these data enable investigations of the REEs' fate during not only early diagenesis but also through the 500 kyr deposition time. Our approach includes (i) the vertical profiles of pore water REEs and other chemical species, (ii) the shale (Post-Archean Australian Shale, PAAS)- and seawater (North Pacific Deep Water, NPDW)-normalized REE patterns, (iii) the production rate calculations and (iv) the upward flux of the dissolved REEs across the sediment–water interface.

## 2. Materials and methods

### 2.1. Study area and sediment composition

The sampling site (U1345) is located on the northeastern continental slope in a highly productive “Green Belt” zone (Springer et al., 1996) (Fig. 1); the primary production is  $>170 \text{ g C m}^{-2} \text{ y}^{-1}$  (Sambrotto et al., 2008). The Bering Slope Current carries nitrate-rich deep waters to the photic zone, and the bottom waters of the outer shelf carry dissolved iron (Hurst et al., 2010), sustaining the high productivity of this zone. The water depth was 1008 m, and the site is in a modern oxygen minimum zone (Takahashi et al., 2011). The lithology contains primarily siliciclastic sediments with varied diatom content (Expedition 323 Scientists, 2011b). The siliciclastic fraction is primarily composed of quartz, feldspar, rock fragments and clay minerals, while pyrite mottles and specks are frequent. Ash was only intermittently observed at Site U1345. The sediments' age was determined onboard using the average last occurrence of *Spongodiscus* sp., and the U1345 sediments included material from the mid-Pleistocene ( $\sim 0.5 \pm 0.1 \text{ Ma}$ ) to the present

(Takahashi et al., 2011). The mean sedimentation rate for the last 300 ka was  $29 \text{ cm ky}^{-1}$  (Takahashi et al., 2011); and the organic carbon burial rate was  $199 \text{ mmol m}^{-2} \text{ y}^{-1}$ , based on the wet bulk density, porosity and total organic carbon content (Wehrmann et al., 2011).

### 2.2. Pore water sampling and onboard geochemical analyses

The sample acquisition and analyses followed the standard ODP protocols (Gieskes et al., 1991; Murray et al., 2000). Sediment depths are reported as the corrected core composite depth below seafloor (CCSF-B), generating a common depth scale for multiple holes and allowing for the calculation of the absolute rates and fluxes (Mix et al., 2003).

Two holes were drilled to ~40 (Hole A) and ~140 (Hole B) mbsf in August 2009. For Hole A, whole rounds for pore water extraction were retrieved at a resolution of two samples per core for the first two cores and one sample per core thereafter (17 total samples). For Hole B, samples were collected at 0.25 m depth intervals for the first 12 mbsf. The sampling interval was increased to 0.7–1.5 m down to 36 mbsf and ~9.5 m thereafter (77 total samples). Whole rounds were stored in an  $\text{N}_2$ -filled glove box at  $7^\circ \text{C}$  until pore water was extracted with Manheim-type hydraulic presses (Manheim et al., 1994). The water samples were filtered immediately using  $0.45 \mu\text{m}$  filters (Expedition 323 Scientists, 2011a). Aliquots for the REE analyses were spiked with  $50 \mu\text{L}$  ultrapure (UP) nitric acid.

On board the JOIDES Resolution, the alkalinity was measured using Gran titration with a Metrohm autotitrator, and dissolved inorganic carbon (DIC) was measured using a UIC 5011  $\text{CO}_2$  coulometer. The  $\text{SO}_4^{2-}$ ,  $\text{Ca}^{2+}$  and  $\text{Mg}^{2+}$  contents were determined with a Dionex ICS-3000 ion chromatograph; the ammonium ( $\text{NH}_4^+$ ) and total hydrogen sulfide contents were measured with a Shimadzu UV mini 1240 UV–Vis spectrometer. The phosphate content was determined with an OI Analytical discrete analyzer (DA3500) spectrophotometer; the Mn, Fe and Ba contents were assessed with a Teledyne Prodigy high-dispersion ICP-AES. High-resolution samples for the hydrocarbon gasses in the top 15 mbsf were collected on the catwalk to minimize loss.

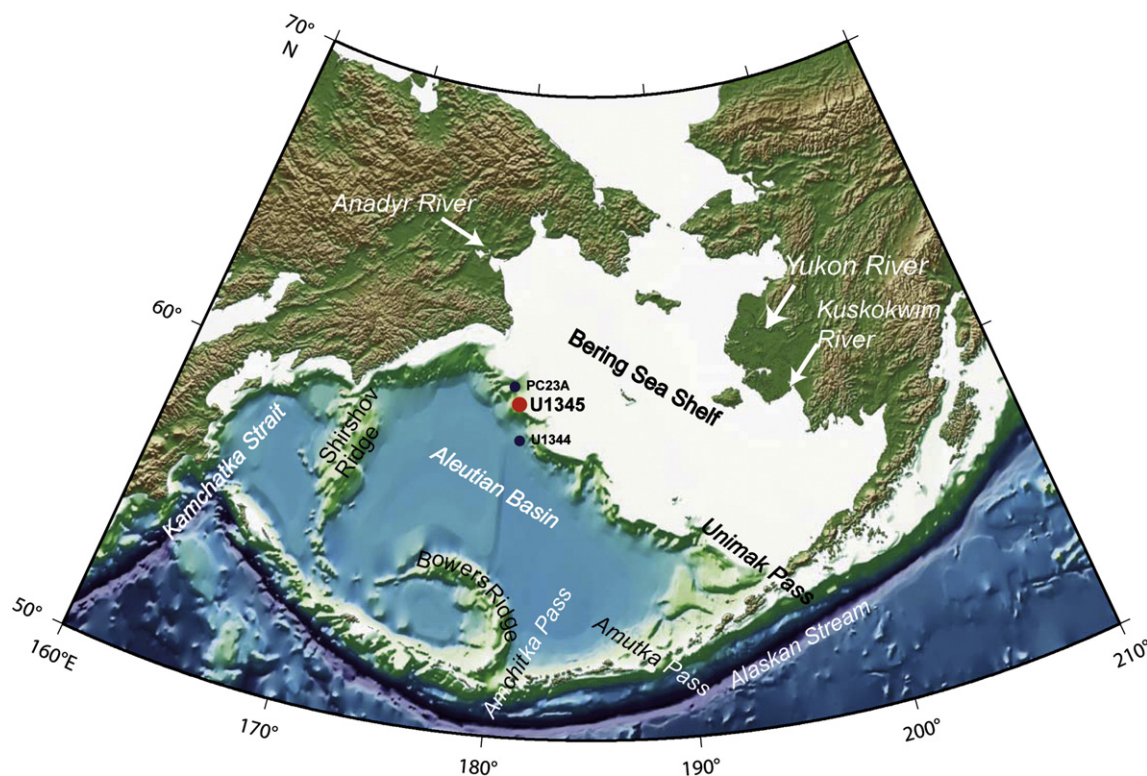


Fig. 1. Map showing the bathymetry and topography of the Bering Sea and surrounding continents. Site U1345 drilled during the Integrated Ocean Drilling Program (IODP) Exp. 323 is marked.

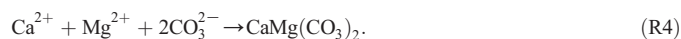
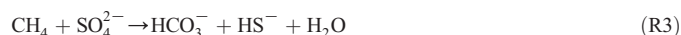
The headspace gas samples were analyzed using an Agilent 6890 gas chromatograph. The data are available in the IODP LIMS database (<http://iodp.tamu.edu/tasapps>).

The downward sequence of the following microbially mediated processes was observed (Expedition 323 Scientists, 2011b; Wehrmann et al., 2011). In the upper 10 m, intense organic carbon mineralization was enabled, yielding high DIC and  $\text{NH}_4^+$  concentrations (Fig. 2), through organoclastic Mn (IV) and sulfate reduction:



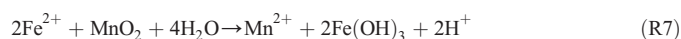
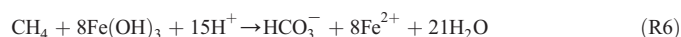
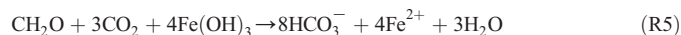
A shallow dissolved Mn peak at 2–4 mbsf most likely resulted from these reactions.

There was a prominent sulfate-methane transition zone (SMTZ) at 6.3 mbsf: the  $\text{SO}_4^{2-}$  drops to zero, the  $\text{CH}_4$  concentrations start to increase and the maximum  $\text{H}_2\text{S}$  is observed (Fig. 2) (Expedition 323 Scientists, 2011b; Wehrmann et al., 2011). The anaerobic oxidation of methane (AOM) is coupled to sulfate reduction (R3), and diagenetic Mg-rich calcite or dolomite forms, subtly decreasing the Ca and Mg contents in the pore waters (R4) (Fig. 2) (Wehrmann et al., 2011):



Biogenic barite forms in the water column and is buried in the sediment; this material dissolves when the sulfate concentrations are low, and diagenetic barite precipitates at higher sediment levels (Jørgensen and Kasten, 2006).

Below the SMTZ, fermentation and subsequent methanogenesis occurred, down to 140 mbsf (Wehrmann et al., 2011). Distinct peaks for dissolved iron (Fe) and manganese (Mn) were observed immediately below the SMTZ in the methanogenesis zone (Fig. 2), while the general early diagenesis sequence places the microbial dissimilatory Fe and Mn reduction (R5 and R1) before the sulfate reduction (R2). At these depths,  $\text{H}_2\text{S}$  was already sequestered; therefore, the reduced Fe species escape precipitation as sulfide intermediates and, ultimately, pyrite. The Fe and Mn peaks may result from iron reduction through the AOM (R6) and  $\text{Fe}^{2+}$  re-oxidation by Mn-oxides (Canfield et al., 1993) (R7) (Expedition 323 Scientists, 2011b). Alternatively, these peaks may result from ferromagnesian silicate mineral dissolution in the anoxic zone.



### 2.3. REE analyses

The preserved pore water samples were transferred to the laboratory at the Seoul National University, and concentrations of 14 REEs were determined. To avoid contamination, all the analytical procedures including sample handling, column separation, evaporation and dilution were carried out on an ULPA-filtered clean bench placed inside a HEPA-filtered clean booth. The experimental tools, including high

density polyethylene and polypropylene bottles, Teflon beakers and columns and polypropylene pipette tips were also cleaned on the class-10 clean bench, according to the protocol described by Soyol-Erdene et al. (2011). UP water was obtained after a three-stage purification process: reverse osmosis (Innovation Human Power 1+, Human Corporation), deionization (Puris Esse UP Basic, Mirae Co.) and trace metal filtration (Protego, Mykrolis Corporation, MA, USA). Commercial UP grade  $\text{HNO}_3$  was used in all the experimental procedures. Single element standard solutions (100 ppm) for the 14 REEs, in addition to Y, Ba and In, were obtained from Perkin-Elmer.

The REEs were separated from the high salinity matrix with a RE-Spec chromatographic extraction resin (100–150 mesh, Eichrom) (Esser et al., 1994). The resin was leached with 0.03 M HF at 60 °C for 24 h, rinsed with UP water several times and leached with UP water at 60 °C for 24 h. The resin was rinsed and stored in UP water. To avoid possible memory effects and obtain the lowest detection limit, the resin was not recycled. To optimize the column separation procedure, we tested various nitric acid concentrations (4, 5, 6 and 8 M) and volumes for column washing, while varying the sample amounts using synthetic REE standard solutions as well as river and seawater certified as reference materials (CRMs). The final analytical procedure used for the pore waters is illustrated in Fig. 3. The pre-cleaned resin (120  $\mu\text{L}$ ) was loaded onto a Saville PFA microcolumn (5 mL, 3.2 mm ID) and rinsed with 3 mL 0.05 M HF and 5 mL 0.015 M  $\text{HNO}_3$ , consecutively. Subsequently, the column was pre-conditioned using 2 mL 6 M  $\text{HNO}_3$ .

Approximately 4.5 mL of pore water was weighed and evaporated to dryness in a pre-cleaned Teflon beaker using a quartz hot plate with a Teflon-coated carbon block. The residue was dissolved in 1 mL of 6 M  $\text{HNO}_3$  and loaded onto a preconditioned column. Subsequently, the column was washed with 100, 100, 100, 200, 200 and 500  $\mu\text{L}$  (total 1200  $\mu\text{L}$ ) of 6 M  $\text{HNO}_3$  sequentially, and the REE fraction was collected in pre-cleaned Teflon beakers with 5 mL of 0.015 M  $\text{HNO}_3$ . After evaporating to dryness, a drop of UP  $\text{HNO}_3$  and 1 mL UP water was added to re-dissolve the samples. Before the instrumental analyses, 50  $\mu\text{L}$  of 10 ng  $\text{mL}^{-1}$  In solution was added as an internal standard to achieve a final concentration of 0.5 ng  $\text{mL}^{-1}$ .

The REE concentrations were measured using a sector field inductively coupled plasma mass spectrometer (ICP-SFMS, Element2, Thermo Finnigan MAT, Germany) coupled to a desolvation nebulization system (Aridus II, Cetac Technologies, USA) installed in a HEPA filtered laboratory at the National Center for Inter-University Research Facilities of Seoul National University. The desolvation system rendered oxide production negligible ( $\text{BaO}/\text{Ba} < 0.02\%$ ). To attain the lowest blank level, UP grade (99.999%) argon and nitrogen gasses were used, and the sample introduction system was placed in an ULPA-filtered laminar flow clean bench. Details of the instrumental operating conditions and data acquisition parameters are provided in Table 1.

The REEs in matrix-separated pore water samples were externally calibrated. Working standard solutions were prepared gravimetrically by sequentially diluting a 10 ppm REE multi-element standard solution with 1% (m/m) UP  $\text{HNO}_3$ ; the standard solution was prepared from 100 ppm single element REE solutions. Instrumental drift was corrected using the In (0.5 ng  $\text{mL}^{-1}$ ) internal standard.

To minimize spectral interference from the light REE (LREE) on the heavy REE (HREE), the instrumental parameters were optimized daily to achieve the lowest oxide production rate and highest sensitivity. Under our instrumental conditions, spectral interference caused by LREE was less than 5%. Therefore, mathematical corrections were not required. The Ba concentrations were very high in pore water samples ( $\sim 20 \mu\text{M}$ ), making it the most likely interferent for La, Ce and Gd; repeated column separation was necessary for some samples (indicated in Tables 2 and 3).

The recovery from the column separation step was evaluated using 100 pg  $\text{mL}^{-1}$  REE multi-element standard solutions. The recoveries



exceeded 90% for every REE except La (80–90%). The accuracy and blank levels for the analytical procedure, including the column separation and instrumental analysis, are given in Table 4. Because no CRMs for pore water are available, riverine and seawater CRMs (SLRS 4 and NASS 5, National Research Council of Canada, Ottawa, Canada) were used to assess the accuracy. The analytical results for every REE as well as Y agreed with those compiled from the literature. Despite the very low REE concentrations in seawater (fM) and the relatively low sample volumes (5 mL), the REE concentrations obtained during this study agreed with literature values (Table 4). The procedural detection limit (three times the standard deviation of 10 blank measurements) after correcting

for the pre-concentration factor (~5), varied between 0.03 (for Ho) and 1 (for La)  $\text{pg mL}^{-1}$  (Table 4).

The accuracy and blank contributions were controlled during every pre-treatment experiment via parallel analyses of CRM (5 mL NASS5) and a blank solution (1 mL 6 M  $\text{HNO}_3$ ). One pre-treatment experiment consisted of ten samples, in addition to one blank and one CRM. The blank levels, including the column separation and instrumental analysis, were not significantly different from the procedural detection limit (Table 4). Therefore, only the instrumental blank was subtracted from the sample signals. The precision for every REE in NASS5 was <10% (fifteen repeated analyses of 5 mL NASS5) (Table 4).

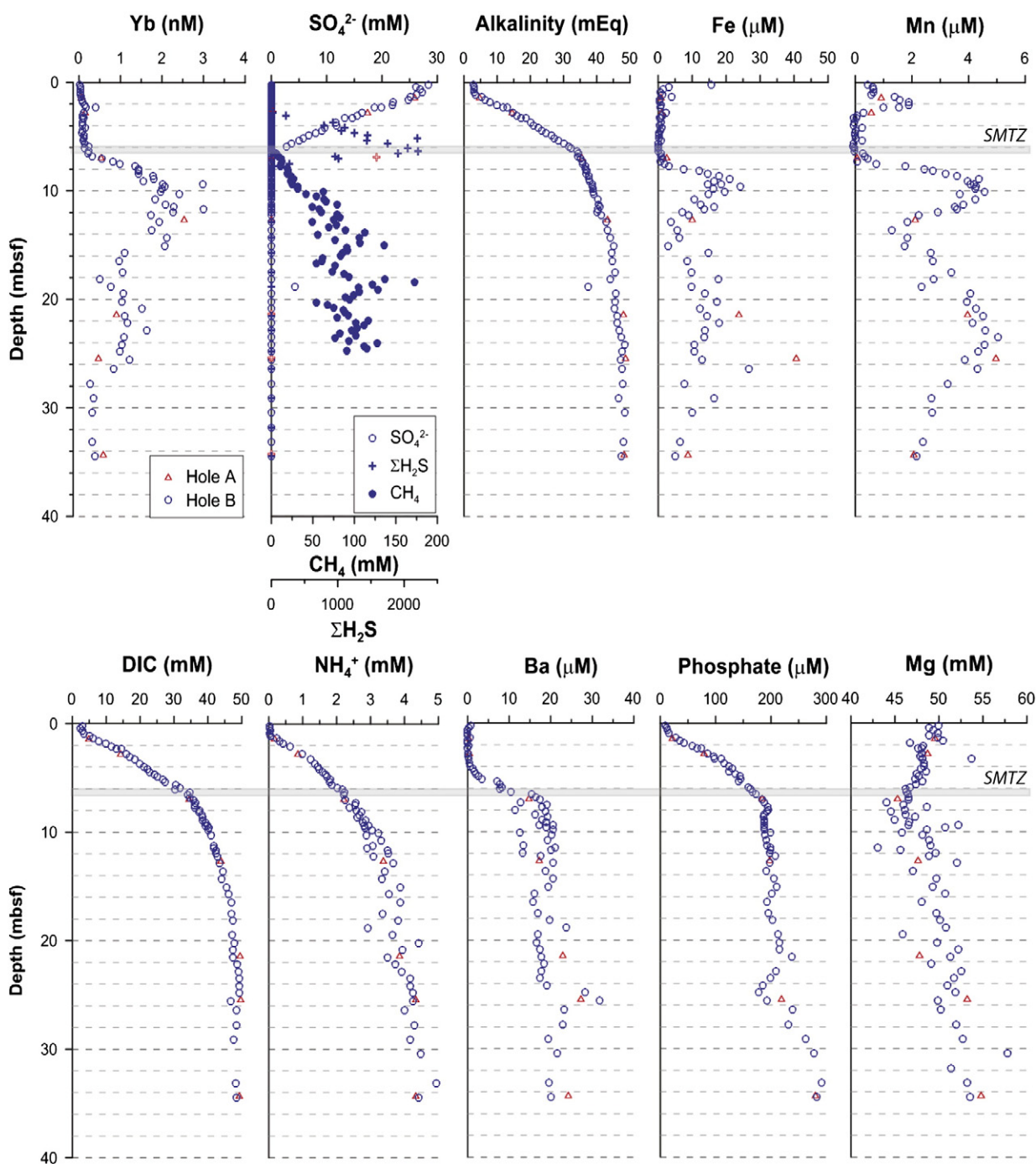


**Fig. 2.** Pore water concentration profiles of Yb as an example of HREE, sulfate ( $\text{SO}_4^{2-}$ ), total hydrogen sulfide ( $\text{H}_2\text{S}$ ), methane ( $\text{CH}_4$ ), alkalinity, iron (Fe), manganese (Mn), dissolved inorganic carbon (DIC), ammonium ( $\text{NH}_4^+$ ), barium (Ba), phosphate and magnesium ( $\text{Mg}^{2+}$ ) (Expedition 323 Scientists, 2011b). The sulfate-methane transition zone (SMTZ) was identified at 6.3 mbsf at this site, based on the concentrations of  $\text{SO}_4^{2-}$  and methane (Wehrmann et al., 2011).

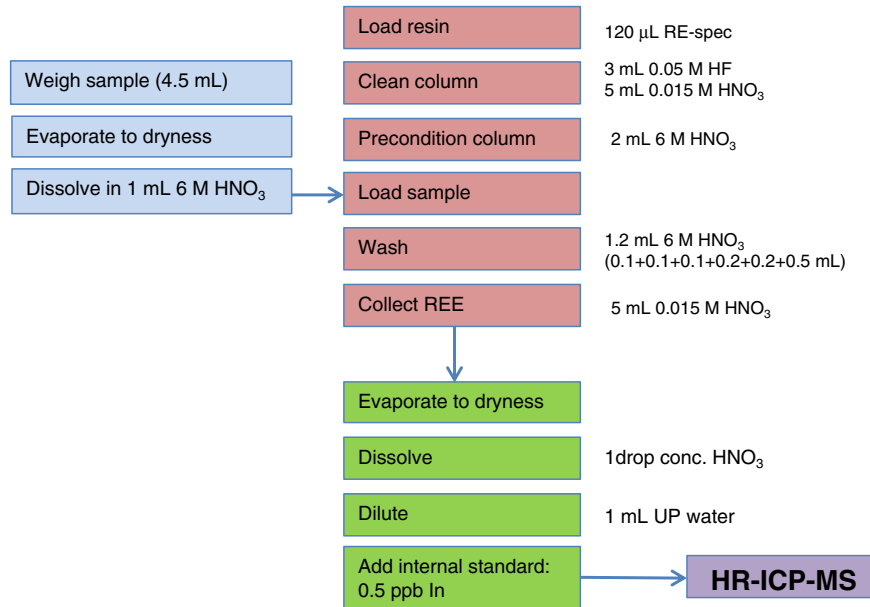


Fig. 3. Column chromatography procedure for REE determination in marine pore water samples.

#### 2.4. Fluxes and reaction rates

The REE flux across the sediment–water interface was calculated using Fick's First Law:

$$J = \phi D_s \frac{\partial C}{\partial x}, \quad (1)$$

where  $J$  is the flux,  $\phi$  is the sediment porosity measured onboard (Expedition 323 Scientists, 2011b) and interpolated as  $0.69 \cdot (x^{-0.05})$ ,  $D_s$  is the temperature-corrected sediment diffusion coefficient (calculated as below and listed in Table 4),  $C$  is the REE concentration in the pore water and  $x$  is the depth (Bernier, 1980). The diffusion coefficients were calculated using  $D_s = D_{sw}/\theta^2$ , where  $D_{sw}$  is the free diffusion coefficient

in seawater ( $\sim 0.92 \times D_0$  at 25 °C) and  $\theta$  is the tortuosity (Li and Gregory, 1974; Boudreau, 1997). The self-diffusion coefficients for the REEs in water ( $D_0$ ) were calculated by applying the equations provided by Li and Gregory (1974). The tortuosity ( $\theta$ ) was calculated as  $\theta^2 = 1 - \ln(\phi^2)$  (Boudreau, 1997). The temperature was corrected for  $D_s$  with the measured geothermal gradient (Expedition 323 Scientists, 2011b).

The reaction rates for LREE (Nd), middle REE (MREE) (Dy), HREE (Yb), Fe, Mn, DIC,  $\text{NH}_4^+$ ,  $\text{Mg}^{2+}$ , Ba and phosphate were quantified with a finite-difference method using numerical solutions from the one-dimensional mass conservation equation:

$$\frac{\partial(\phi C)}{\partial t} = \frac{\partial}{\partial x} \left[ \frac{D}{\phi f} \frac{\partial(\phi C)}{\partial x} - (\phi b + \phi v) C \right] + R(x) = 0, \quad (2)$$

where  $b$  is the pore water burial velocity,  $v$  is the externally driven flow rate,  $f$  is the formation factor measured onboard (Expedition 323 Scientists, 2011a) and  $R$  is the net rate of solutes produced (or consumed if  $R$  is negative) per unit volume of sediment (Wang et al., 2008). Production (increased pore water concentration) and consumption (decreased pore water concentration) arise from processes besides diffusion and advection, including dissolution–precipitation and adsorption–desorption. The rates were modeled for the upper 40 mbsf of Holes A and B. The three samples in the first meter were excluded due to problems with data that were most likely due to compaction or other sampling artifacts. A 5-point Gaussian filter was applied to the concentration, formation factor and porosity data. The minimum number of concentration data points in each zone was 9, and a significance level of 0.05 was used during the F test. For Mg, the minimum number of concentration data points for each zone was 5 because the data were scattered. Compaction was neglected, the sedimentation rate near the seafloor was assumed to be  $2.9 \cdot 10^{-4} \text{ m}^2 \text{ y}^{-1}$  and the externally driven flow rate near the seafloor was  $1 \cdot 10^{-5} \text{ m}^2 \text{ y}^{-1}$  (Wang et al., 2008; Takahashi et al., 2011). Varying the advection rate to  $1 \cdot 10^{-4} \text{ m}^2 \text{ y}^{-1}$  did not appreciably change the reaction rates ( $\sim 8\%$  on average). For the Monte Carlo estimation of uncertainty, we used the relative precision of the concentration measurements (0.01) and the number of random concentration profiles (50). The uncertainties are given as the horizontal thickness of the bars in Figs. 5 and 6.

Table 1

Instrumental conditions and measurement parameters for the SF-ICPMS and the desolvation system.

Gas flow rates	
Cool/L min <sup>-1</sup>	16.00
Auxiliary/L min <sup>-1</sup>	0.50–0.90 <sup>a</sup>
Sample/L min <sup>-1</sup>	0.80–1.00 <sup>a</sup>
Sweep gas/L min <sup>-1</sup>	2.8–3.3 <sup>a</sup>
Nitrogen flow rate/mL min <sup>-1</sup>	2–7 <sup>a</sup>
Membrane temperature/°C	160
Spray chamber temperature/°C	110
Washing time/min	2
Take up time/s	40
Selected isotopes	<sup>137</sup> Ba, <sup>89</sup> Y, <sup>139</sup> La, <sup>140</sup> Ce, <sup>141</sup> Pr, <sup>146</sup> Nd, <sup>147</sup> Sm, <sup>151</sup> Eu, <sup>158</sup> Gd, <sup>159</sup> Tb, <sup>161</sup> Dy, <sup>165</sup> Ho, <sup>166</sup> Er, <sup>169</sup> Tm, <sup>171</sup> Yb, <sup>175</sup> Lu
Resolution	Low ( $m, \Delta m^{-1} = 300$ )
Dwell time per acquisition point/ms	5
No. of acquisition points per mass segment (sample per peak)	100
Total acquisition time (per mass segment)/s	0.25
Acquisition window (%)	50
Search window (%)	50
Integration window (%)	20

<sup>a</sup> Optimized to maximize intensity and minimize oxide production.

**Table 2**  
Concentrations of REEs (pM) in pore waters of Hole A.

Depth (mbsf)	Y	La	Ce	Pr	Nd	Sm	Eu	Gd	Tb	Dy	Ho	Er	Tm	Yb	Lu	Yb <sub>n</sub> /Nd <sub>n</sub> <sup>a</sup>	MREE/MREE <sup>*a,b</sup>	Ce/Ce <sup>*a,c</sup>
1.32	815	195	384	41.3	165	39.3	10.4	53.6	8.24	57.3	13.8	46.6	7.27	51.9	9.80	4.53	1.02	1.10
2.74	2030	102	233	30.4	152	46.7	13.7	81.9	15.7	132	37.1	138	22.3	159	27.4	15.1	0.88	1.27
6.93	4270	193	630	80.7	342	88.5	24.4	129	28.5	253	79.2	335	64.3	540	113	22.8	0.51	0.99
12.60	16200	181	487	66.6	333	106	34.3	245	75.5	881	321	1511	296	2530	522	110	0.39	1.21
21.35	5580	158	559	71.6	317	87.4	26.1	132	30.3	308	111	509	103	910	205	41.3	0.37	1.05
25.34	3250	67.9	197	26.1	128	41.0	12.2	75.3	17.3	178	61.4	281	55.2	468	95.8	52.8	0.42	1.20
34.28	4230	179	605	78.8	346	98.9	28.6	147	27.0	235	74.9	337	66.3	585	129	24.4	0.44	1.02
44.22	5250	137	419	55.2	271	82.2	23.7	133	27.9	263	88.3	403	79.6	694	151	37.0	0.42	1.21
52.32	2000	58.8	142	16.7	77.9	22.3	6.24	34.6	7.26	90.4	41.0	226	49.9	449	104	83.1	0.22	1.24
62.94	2900	93.4	259	34.3	175	56.2	16.2	92.2	18.0	166	55.0	251	50.4	434	94.1	35.7	0.42	1.30
72.55	2750	63.9	221	28.0	138	41.0	12.4	69.1	16.3	137	49.8	242	51.7	478	107	50.1	0.32	1.26
81.96	2590	162	561	61.0	260	67.9	18.8	95.9	17.3	139	41.2	182	36.2	319	73.5	17.7	0.47	1.17
91.92	2030	n.d.	285	33.9	164	47.4	14.0	77.5	17.1	124	38.3	171	35.4	319	72.4	28.2	0.43	1.30
99.88	1280	27.3	59.8	9.68	51.8	16.9	5.09	31.8	7.90	63.8	22.5	111	24.7	232	55.1	64.5	0.31	1.19
110.35	1880	99.4	197	35.3	168	47.9	13.7	71.8	15.0	111	31.4	128	25.3	218	47.9	18.7	0.54	0.84
119.52	1220	56.0	155	19.1	86.5	24.5	7.10	37.6	7.06	61.6	19.8	94.0	20.0	189	45.1	31.5	0.36	1.13
129.08	714	62.9	170	18.9	83.5	21.6	5.57	30.3	5.13	39.2	11.9	54.4	11.6	106	25.9	18.3	0.40	1.22
138.74	1430	111	231	31.7	161	46.9	13.2	72.3	12.3	92.1	25.1	101	19.6	171	40.0	15.4	0.57	1.24

*Italics indicate repeated column separation due to very high Ba concentrations.*

<sup>a</sup> Ratios are shale (PAAS)-normalized values.

<sup>b</sup> MREE/MREE<sup>\*</sup> = 2Dy<sub>n</sub>/(Nd<sub>n</sub> + Yb<sub>n</sub>).

<sup>c</sup> Ce/Ce<sup>\*</sup> = Ce<sub>n</sub>/(2Pr<sub>n</sub> - Nd<sub>n</sub>).

### 3. Results

#### 3.1. REE concentration profiles

The REEs are classified into three groups: LREE (La, Ce, Pr and Nd), MREE (Eu, Gd, Tb and Dy) and HREE (Er, Tm, Yb and Lu). The data for Nd, Dy and Yb represent the three groups.

The REE concentrations in the pore water from Holes A and B are listed in Tables 2 and 3, respectively, as well as in Fig. 4. On average, the REE content was higher in the pore water than in the seawater by an order of magnitude for LREE and by two orders of magnitude for HREE, indicating that there was significant liberation from the sediment during diagenesis, especially for the HREEs (Fig. 4). Concentrations of LREE and MREE varied with depth, the max/min molar concentration ratios varying across the series: e.g., 22 for Nd<sub>max</sub>/Nd<sub>min</sub> and 29 for Dy<sub>max</sub>/Dy<sub>min</sub>. The HREE displayed larger variability in the max/min molar concentration ratios (126 for Yb<sub>max</sub>/Yb<sub>min</sub>).

Due to the low sampling resolution of Hole A, only a peak between 7 and 21 mbsf was observed for MREE and HREE in an otherwise constant profile. Hole B was sampled at a higher resolution; the major peak observed for Hole A was located at 9 to 13 mbsf, and the maximum HREE concentrations reached 0.86 nM and 3.0 nM for Dy and Yb, respectively. The yttrium (Y) concentration also reached its maximum (20 nM) within that depth interval; Y displays chemical behavior similar to HREE (especially Ho due to similar ionic radii). In addition, two features that were not detected in the Hole A profiles were observed: a small peak at ~2.5 mbsf and a broad shoulder below the main peak at 18–24 mbsf. The 9-point mean calculated for the finite difference advection diffusion model (Wang et al., 2008) located the major peak at 8–12, the minor peak at 2–4 and the shoulder at 16–24 mbsf (Fig. 5); we will refer to these features as Peak 1 (2 m), Peak 2 (10 m) and the Shoulder (20 m) consecutively with depth. The magnitude of these peaks decreased as the atomic number decreased, dwindling to scattered points for the LREEs and implying a systematic fractionation within the REE series (Fig. 4).

For comparison to the REEs, concentration profiles of alkalinity, Fe, Mn, DIC, NH<sub>4</sub><sup>+</sup>, Ba, phosphate and Mg<sup>2+</sup> (Fig. 2) are also displayed for the top 40 mbsf (Expedition 323 Scientists, 2011b). The depth profiles for Fe and Mn are similar, displaying two peaks (~10 and ~24 mbsf) with an additional Mn peak at ~2 mbsf. The concentrations of alkalinity, DIC, NH<sub>4</sub><sup>+</sup> and phosphate significantly increased in the upper ~10 mbsf

due to active organic matter degradation. Further down, NH<sub>4</sub><sup>+</sup> steadily increased, while alkalinity, DIC and phosphate maintained relatively high concentrations. The dissolved Ba concentration increased from ~5 mbsf just above the SMTZ and demonstrated the largest increase between 5 and 9 mbsf (Expedition 323 Scientists, 2011b; Wehrmann et al., 2011). Below this depth, the Ba concentration remained higher and more consistent. The dissolved Mg content exhibited a scattered distribution but decreased in the upper ~8 m overall before increasing to higher values than in the topmost layer.

Peak 1 coincided with the peak in dissolved Mn, while Peak 2 and the Shoulder matched the peaks in dissolved Fe and Mn below the SMTZ in the methanogenesis zone. Peak 2 seemed to shift slightly deeper in the following order: Fe, Mn, HREE, MREE to LREE.

#### 3.2. Production rate

To identify the depth intervals objectively with respect to the REE production or consumption, we used the numerical model developed by Wang et al. (2008). Based on modeling results, the main REE production and consumption were confined to the top ~40 mbsf of the sediment. Five statistically significant reaction intervals were identified for Nd, as well as seven and eight for Dy and Yb, respectively (Fig. 5). The reaction rates for other major pore water constituents were also calculated for comparison (Fig. 6).

For Peak 1, the net dissolved REE production occurred near the seafloor, at 1–3 mbsf:  $2 \cdot 10^{-10}$  mol m<sup>-3</sup> y<sup>-1</sup> for Nd, Dy and Yb (Fig. 5). Mn ( $3 \cdot 10^{-6}$  mol m<sup>-3</sup> y<sup>-1</sup>), DIC, NH<sub>4</sub><sup>+</sup>, Ba and phosphate production also occurred within this interval, but Fe was consumed. Iron production occurred lower in the sediment column at 3–5 mbsf ( $3 \cdot 10^{-6}$  mol m<sup>-3</sup> y<sup>-1</sup>) (Fig. 6). Immediately below the production zone was a consumption zone (broadly 3–8 mbsf) for REE ( $-8 \cdot 10^{-11}$  mol m<sup>-3</sup> y<sup>-1</sup> for Nd,  $-1 \cdot 10^{-10}$  mol m<sup>-3</sup> y<sup>-1</sup> for Dy and  $-4 \cdot 10^{-10}$  mol m<sup>-3</sup> y<sup>-1</sup> for Yb), Fe ( $-1 \cdot 10^{-5}$  mol m<sup>-3</sup> y<sup>-1</sup>) and Mn ( $-1 \cdot 10^{-6}$  mol m<sup>-3</sup> y<sup>-1</sup>).

For Peak 2, net production occurred at 8–12 mbsf for Yb ( $3-5 \cdot 10^{-10}$  mol m<sup>-3</sup> y<sup>-1</sup>) and at 8–14 mbsf for Dy ( $2 \cdot 10^{-10}$  mol m<sup>-3</sup> y<sup>-1</sup>), as well as for Fe (8–10 mbsf,  $1 \cdot 10^{-5}$  mol m<sup>-3</sup> y<sup>-1</sup>), Mn (7–12 mbsf,  $0.7-1 \cdot 10^{-6}$  mol m<sup>-3</sup> y<sup>-1</sup>), Mg<sup>2+</sup> (11–13 mbsf) and alkalinity (8–10 mbsf). The consumption zones occurred both above and below this production zone. For the Shoulder, no significant additional REE production zone was evident.

Table 3

Concentrations of REEs (pM) in pore waters of Hole B.

Depth (mbsf)	Y	La	Ce	Pr	Nd	Sm	Eu	Gd	Tb	Dy	Ho	Er	Tm	Yb	Lu	Yb <sub>n</sub> /Nd <sub>n</sub> <sup>a</sup>	MREE/MREE <sup>*a,b</sup>	Ce/Ce <sup>*a,c</sup>
0.24	440	97.0	206	24.4	104	24.4	6.53	30.4	4.60	30.6	6.98	22.6	3.39	23.8	4.31	3.29	1.11	1.09
0.43	729	n.d.	266	27.7	112	20.3	5.51	n.d.	5.45	41.0	11.1	36.9	5.78	42.5	6.98	5.45	0.92	1.15
0.66	601	120	266	32.9	132	29.5	7.38	38.2	6.06	38.7	9.14	29.5	4.46	31.9	5.46	3.47	1.07	0.96
0.90	633	118	240	30.7	125	30.0	8.20	42.4	6.04	44.2	10.6	31.3	4.51	29.6	4.65	3.40	1.31	0.94
1.14	760	177	424	52.6	231	53.2	12.9	65.2	9.66	61.5	13.4	40.3	5.92	37.4	5.83	2.33	1.30	1.07
1.37	925	202	444	53.3	227	56.5	14.0	68.8	10.3	70.4	16.3	53.8	8.44	59.9	10.6	3.80	1.05	1.07
1.66	1013	130	314	40.0	185	47.1	12.3	63.9	10.1	74.8	18.8	64.2	10.0	69.5	11.5	5.42	1.03	1.13
1.85	1102	81.9	188	22.9	109	31.3	9.14	53.4	9.26	71.2	19.7	71.1	11.6	82.2	15.0	10.8	0.90	1.25
2.08	1850	152	319	38.0	176	47.7	13.9	80.4	14.4	118	32.7	119	19.4	143	24.1	11.7	0.86	1.20
2.32	5646	n.d.	754	98.0	375	72.3	20.5	n.d.	29.1	267	87.5	329	53.8	398	70.6	15.3	0.71	0.87
2.32	2369	91.3	252	29.1	138	43.5	13.1	73.2	14.1	126	37.4	138	22.5	167	29.8	17.5	0.80	1.31
2.79	1477	78.9	193	24.6	116	33.4	9.94	54.5	9.87	85.8	24.4	91.9	15.9	120	22.1	15.0	0.76	1.15
3.07	840	53.2	145	17.1	68.3	17.3	5.64	31.2	5.97	50.2	14.2	56.0	10.0	80.3	16.1	17.0	0.67	1.00
3.26	2128	n.d.	203	20.4	92.9	25.9	7.72	41.4	7.54	65.3	19.2	77.1	13.9	114	22.0	17.7	0.61	1.39
3.26	816	77.0	184	25.3	110	28.0	8.19	39.1	6.98	54.5	14.8	56.8	10.0	81.1	16.5	10.7	0.70	0.95
3.73	761	56.0	211	24.3	103	28.8	8.15	40.0	7.67	56.1	15.2	55.2	9.80	79.6	15.7	11.1	0.73	1.10
3.97	852	77.8	214	23.6	103	26.6	7.62	41.1	9.13	60.2	16.0	61.2	11.0	90.0	18.5	12.6	0.70	1.20
4.21	1942	n.d.	388	37.1	166	34.2	10.1	n.d.	12.5	102	31.1	113	18.6	147	27.2	12.7	0.73	1.43
4.49	836	72.2	227	23.5	96.1	24.3	7.44	35.3	7.72	55.3	15.8	58.5	10.1	80.5	17.0	12.1	0.72	1.16
4.68	641	46.4	82.1	8.2	35.1	9.4	3.53	18.0	3.59	34.2	11.2	48.1	8.97	73.8	14.8	30.3	0.51	1.30
4.92	1257	94.0	226	27.2	135	39.3	11.3	62.0	11.0	87.2	23.4	87.2	15.2	115	22.3	12.3	0.79	1.35
5.15	1114	52.5	154	16.0	71.5	20.6	6.47	34.8	6.63	63.4	19.4	80.4	14.8	122	24.8	24.7	0.56	1.31
5.39	899	87.9	303	37.9	165	40.5	9.88	47.5	7.98	61.2	16.6	65.9	11.7	97.6	19.6	8.51	0.63	1.06
5.91	1052	63.0	234	25.9	99.4	26.7	8.69	40.9	10.3	72.3	21.0	86.0	16.1	132	28.0	19.1	0.59	1.02
6.10	1853	n.d.	248	25.6	120	24.7	7.50	n.d.	10.6	94.8	33.2	143	27.7	242	50.1	29.0	0.43	1.43
6.33	1084	64.0	188	22.0	100	29.6	9.10	48.7	9.44	77.5	22.1	87.9	16.1	132	26.0	19.1	0.63	1.20
6.57	2792	158	402	71.6	311	86.0	28.5	128	22.8	177	46.9	173	30.0	231	44.1	10.7	0.79	0.73
6.80	1215	53.6	137	14.6	66.3	19.4	5.27	31.6	8.05	75.0	26.4	120	24.5	215	44.2	46.8	0.39	1.30
7.04	1731	51.9	163	18.0	70.0	19.6	6.14	34.5	9.08	97.2	35.8	173	35.9	322	68.9	66.4	0.34	1.04
7.32	3098	89.0	150	18.1	81.8	24.2	7.81	50.2	14.5	166	62.1	299	61.5	551	114	97.2	0.34	1.15
7.51	5069	77.0	230	29.7	143	44.9	14.8	93.4	26.8	282	101	465	94.6	824	175	82.8	0.38	1.20
7.75	5595	50.6	187	22.6	97.6	30.3	10.8	72.5	23.9	296	113	537	111	984	211	145	0.34	1.08
7.99	9432	n.d.	273	27.3	121	24.7	9.05	n.d.	28.2	356	162	776	152	1351	282	161	0.30	1.35
8.18	7979	65.9	222	28.0	122	38.8	15.2	92.4	36.0	420	169	783	160	1443	314	171	0.33	1.04
8.42	8310	84.3	260	34.8	149	45.8	15.7	106	35.3	433	166	793	166	1436	299	139	0.34	0.97
8.65	9153	119	407	48.4	202	59.5	18.9	126	40.2	464	175	821	169	1441	304	103	0.36	1.05
8.89	10905	99.3	282	37.0	183	60.9	20.8	148	47.4	568	216	1022	205	1785	364	141	0.36	1.24
9.12	10762	122	298	41.2	204	62.2	19.9	152	50.1	595	224	1042	210	1800	351	127	0.37	1.18
9.41	8758	274	628	97.3	446	113	30.9	178	47.8	534	193	882	180	1547	305	50.1	0.38	0.91
9.60	13405	77.2	291	37.0	176	62.4	23.8	160	55.7	677	257	1194	236	2018	417	165	0.38	1.19
9.83	20092	n.d.	491	57.3	263	66.2	23.5	n.d.	70.0	864	368	1706	343	2980	593	163	0.33	1.22
10.07	15402	268	774	114	560	168	47.4	301	76.3	824	288	1293	257	2075	406	53.4	0.44	1.10
10.31	13074	92.2	325	41.9	183	66.6	24.1	166	55.7	678	253	1159	237	1995	400	157	0.38	1.02
10.54	13709	137	496	65.5	292	94.8	30.8	206	63.5	719	263	1199	239	1966	398	97.1	0.41	1.03
10.82	14615	n.d.	302	39.9	195	65.2	22.4	170	60.0	751	289	1382	278	2416	478	178	0.35	1.21
11.01	10063	50.9	180	22.0	103	31.9	12.4	93.0	39.0	508	206	1011	207	1827	381	256	0.31	1.20
11.25	12905	83.8	207	28.0	144	49.9	17.5	148	54.8	691	265	1257	251	2093	426	210	0.37	1.28
11.49	15086	82.8	302	39.1	192	69.7	26.6	193	67.7	815	303	1383	271	2291	468	172	0.40	1.23
11.72	20847	n.d.	321	33.4	165	35.2	14.6	n.d.	52.0	697	332	1642	334	3006	629	263	0.26	1.54
11.96	15931	165	382	55.6	265	85.2	28.1	209	66.5	801	299	1380	277	2269	458	124	0.40	1.04
12.24	10142	90.9	287	38.9	159	45.8	15.5	111	41.3	524	204	972	203	1732	362	157	0.34	0.90
12.90	12612	122	442	57.8	238	78.3	27.8	175	56.5	656	244	1121	231	1935	403	117	0.38	0.93
13.66	12291	357	963	144	782	216	54.3	334	76.5	772	260	1120	216	1752	328	32.3	0.48	1.34
14.32	14424	214	539	75.8	361	114	36.1	241	71.4	788	281	1286	250	2111	414	84.3	0.42	1.07
15.08	12948	95.9	254	34.8	177	63.2	22.7	178	61.0	727	272	1242	250	2067	410	169	0.40	1.24
15.74	6421	64.8	177	22.9	110	33.9	11.2	83.3	27.9	342	131	611	127	1108	234	145	0.35	1.18
16.49	6901	n.d.	369	44.7	176	31.3	8.35	n.d.	19.4	227	106	509	102	963	249	78.9	0.26	0.96
17.50	6501	180	637	82.1	385	111	30.3	158	37.0	361	133	575	117	1051	224	39.4	0.38	1.14
18.14	5719	196	678	107	513	155	41.0	230	41.4	332	93.5	353	63.4	497	97.6	14.0	0.71	0.96
18.86	4921	115	353	46.7	208	62.7	19.1	104	26.2	269	94.6	430	88.0	763	158	53.0	0.39	1.02
19.49	5711	84.7	243	29.8	142	42.5	12.6	80.7	25.1	292	115	577	120	1077	227	110	0.30	1.23
20.20	5527	83.1	269	30.0	124	33.8	10.0	62.2	21.5	264	109	549	115	1027	222	119	0.29	1.10
20.83	7539	33.4	83.2	11.4	63.9	25.8	9.49	70.2	28.2	370	151	741	166	1527	295	345	0.27	1.61
21.54	6553	126	468	65.4	292	80.2	22.4	127	32.2	344	130	611	125	1106	243	54.6	0.35	0.97
22.17	8730	n.d.	352	39.6	185	36.9	11.5	n.d.	23.8	286	131	636	125	1170	287	91.3	0.27	1.29
22.88	9562	41.8	102	15.0	84.8	34.9	12.5	90.4	31.4	434	176	859	189	1643	314	279	0.30	1.51
23.51	7303	310	787	114	544	148	37.2	214	42.5	404	138	631	126	1085	236	28.8	0.41	1.05
24.22	10039	292	961	153	788	244	64.1	360	66.8	567	168	680	128	1032	207	18.9	0.59	1.11
25.56	5969	144	439	55.5	246	69.9	19.6	113	26.7	287	108	532	109	993	212	58.3	0.32	1.07
26.45	7632	123	384	48.1	227	70.7	21.2	130	34.0	366	136	664	136	1224	258	77.6	0.33	1.19
27.79	5875	191	798	105	476	129	34.9	177	36.9	321	105	468	93.5	827	180	25.0	0.42	1.05



Table 3 (continued)

Depth (mbsf)	Y	La	Ce	Pr	Nd	Sm	Eu	Gd	Tb	Dy	Ho	Er	Tm	Yb	Lu	Yb <sub>n</sub> /Nd <sub>n</sub> <sup>a</sup>	MREE/MREE <sup>a,b</sup>	Ce/Ce <sup>a,c</sup>
33.15	3285	137	333	41.4	191	49.3	17.2	76.9	15.3	133	42.7	181	36.4	313	63.6	23.6	0.46	1.15
34.49	3948	259	842	106	421	112	30.1	148	26.3	204	57.4	233	44.1	379	77.7	13.0	0.57	0.93

*Italics* indicate repeated column separation due to very high Ba concentrations.

n.d.: no data. Data was excluded due to contamination.

<sup>a</sup> Ratios are shale (PAAS)-normalized values.

<sup>b</sup> MREE/MREE<sup>\*</sup> = 2Dy<sub>n</sub>/(Nd<sub>n</sub> + Yb<sub>n</sub>).

<sup>c</sup> Ce/Ce<sup>\*</sup> = Ce<sub>n</sub>/(2Pr<sub>n</sub> - Nd<sub>n</sub>).

### 3.3. REE pattern

The PAAS-normalized REE patterns (Taylor and McLennan, 1995) were all HREE-enriched with a slight MREE bulge for a few near-surface samples. Fig. 7 displays the patterns for the different depth intervals: the shallow production zone (1–3 mbsf), the shallow sink zone (3–8 mbsf), the main production zone (8–12 mbsf) and the minor sink zone (12–18 mbsf).

To discuss the REE patterns more quantitatively, we adopted three parameters: the HREE enrichment, the MREE bulge and the Ce anomaly. The magnitude of the HREE enrichment, expressed as the Yb<sub>n</sub>/Nd<sub>n</sub> ratio, varied widely (hereafter, a subscripted n indicates normalization to PAAS). However, at every depth except for the top ~1 m, there was HREE-enrichment relative to the PAAS. The Yb<sub>n</sub>/Nd<sub>n</sub> ratio attained its maximum (up to 263) at Peak 2 (Fig. 8). The MREE bulge was calculated as 2Dy<sub>n</sub>/(Nd<sub>n</sub> + Yb<sub>n</sub>) and was the largest in the uppermost pore waters (Figs. 7 and 8). There was no pronounced Ce anomaly (Ce/Ce<sup>\*</sup> = Ce<sub>n</sub>/(2Pr<sub>n</sub> - Nd<sub>n</sub>)) in the PAAS-normalized pattern (average Ce/Ce<sup>\*</sup><sub>PAAS</sub> = 1.1 ± 0.2) (Figs. 7 and 8). The NPDW-normalized patterns exhibited a distinct positive Ce anomaly that was constant across different depths (average Ce/Ce<sup>\*</sup><sub>NPDW</sub> = 10.1 ± 1.1).

### 3.4. REE flux from sediment to seawater

A significant upward flux of REEs from the subsurface sediment to open seawater was expected due to the high concentration gradient between the pore water and the seawater (Elderfield and Sholkovitz, 1987; Sholkovitz et al., 1989; Schacht et al., 2010). The higher REE concentrations found in deep seawater relative to surface seawater are sometimes attributed to this flux (Shimizu et al., 1994). Alternatively,

the remineralization of settling particles would be highly likely in an oxygen minimum zone and may account for the nutrient-like profiles of REE in seawater (Nozaki, 2001). REE concentrations in the uppermost pore water sample (0.24 mbsf) were 2.5 (for La)–5.4 (for Sm) times higher than NPDW (except 52 times for Ce). Assuming that the REE concentration gradient between the uppermost pore water sample (0.24 mbsf) and bottom seawater (average NPDW) support a diffusive flux, we calculated diffusion fluxes between 0.003 nmol m<sup>-2</sup> y<sup>-1</sup> (for Tm) and 0.29 nmol m<sup>-2</sup> y<sup>-1</sup> (for Ce) (Table 5, Fig. 9). For comparison, we calculated the fluxes for the Cascadia margin (Kim et al., 2012), California margin and Nazca Ridge (Haley et al., 2004) as well as for Buzzards Bay (Elderfield and Sholkovitz, 1987; Sholkovitz et al., 1989) and the Niger Delta (Bayon et al., 2011b) using the same temperature-corrected sediment diffusion coefficients as the Bering Sea site (the temperature was assumed to be 2.89 °C) and assuming a 74% porosity (Table 5, Fig. 9). Earlier calculations of the REE flux for the Buzzards Bay (Elderfield and Sholkovitz, 1987) were likely over-estimated because the assigned values for the diffusion coefficient were rather high (D<sub>s</sub> = 3 × 10<sup>-2</sup> m<sup>2</sup> y<sup>-1</sup> versus 0.4 × 10<sup>-2</sup> m<sup>2</sup> y<sup>-1</sup> in this study) and the sediment porosity was ignored. Upward REE fluxes at different geographic locations range over several orders of magnitude, while the patterns remained relatively flat (Fig. 9). The fluxes at the Bering Sea Slope and Cascadia margin were the lowest. There is a caveat for this comparison: for all the other literature-based calculations, diffusion fluxes were determined over a vertical distance of less than 1.5 cm, while for the Bering Sea Slope and the Cascadia margin the distances were 24 cm and 73 cm, respectively. Therefore, in the latter cases, the fluxes were averaged over longer intervals, but the actual fluxes might only occur over a narrow sub-interval.

Table 4

REE concentrations (pg mL<sup>-1</sup>) in seawater (NASS5) and river water (SLRS4) certified reference materials.

REE	Blank level <sup>a</sup>	Detection limit <sup>b</sup>	D <sub>s</sub> (25 °C) <sup>c</sup> m <sup>2</sup> y <sup>-1</sup>	NASS5						SLRS0034	
				This study <sup>b</sup>	Willie and Sturgeon (2001)	Shaw et al. (2003)	Bayon et al. (2011a)	Freslon et al. (2011)	Lawrence and Kamber (2007)	This study <sup>d</sup>	Compiled <sup>e</sup>
Y	0.1	0.2	0.00874	19.5 ± 1.0	–	–	26 ± 1	25 ± 1	22 ± 2.9	147	146 ± 8
La	0.6	1.0	0.00898	10.3 ± 0.9	12.8 ± 1.2	12.1 ± 0.5	13 ± 0.4	11.2 ± 0.9	12.19 ± 1.14	260	287 ± 8
Ce	0.5	0.9	0.00896	5.89 ± 0.54	4 ± 0.6	4.5 ± 0.7	5.55 ± 0.11	5.4 ± 0.2	5.72 ± 0.69	335	36 ± 12
Pr	0.04	0.1	0.00891	1.91 ± 0.10	1.5 ± 0.2	2 ± 0.2	2.11 ± 0.05	1.98 ± 0.07	2.09 ± 0.19	66.4	69.3 ± 1.8
Nd	0.1	0.3	0.00889	7.75 ± 0.42	9.9 ± 1.8	8.9 ± 0.5	8.8 ± 0.3	8.4 ± 0.2	8.43 ± 0.65	266	269 ± 14
Sm	0.04	0.1	0.00885	4.27 ± 0.23	4 ± 0.4	4.5 ± 0.2	4.84 ± 0.11	4.7 ± 0.2	4.74 ± 0.34	60.1	57.4 ± 2.8
Eu	0.01	0.1	0.00883	0.30 ± 0.02	0.24 ± 0.05	0.27 ± 0.03	0.305 ± 0.014	0.32 ± 0.02	0.33 ± 0.03	8.35	8 ± 0.6
Gd	0.1	0.5	0.00881	1.75 ± 0.14	1.53 ± 0.28	1.6 ± 0.08	1.9 ± 0.07	1.83 ± 0.15	1.83 ± 0.15	43.8	34.2 ± 2
Tb	0.1	0.3	0.00879	0.24 ± 0.01	0.29 ± 0.05	0.21 ± 0.04	0.283 ± 0.006	0.27 ± 0.01	0.27 ± 0.03	4.59	4.3 ± 0.4
Dy	0.1	0.2	0.00877	1.74 ± 0.11	1.61 ± 0.17	1.78 ± 0.07	1.93 ± 0.07	1.86 ± 0.05	1.82 ± 0.2	25.5	24.2 ± 1.6
Ho	0.01	0.02	0.00875	0.43 ± 0.02	0.36 ± 0.05	0.37 ± 0.04	0.48 ± 0.02	0.47 ± 0.04	0.47 ± 0.06	5.16	4.7 ± 0.3
Er	0.02	0.1	0.00873	1.39 ± 0.05	1.31 ± 0.21	1.37 ± 0.03	1.5 ± 0.03	1.47 ± 0.04	1.43 ± 0.2	14.3	13.4 ± 0.6
Tm	0.01	0.03	0.00871	0.19 ± 0.01	0.15 ± 0.03	0.15 ± 0.03	–	–	0.21 ± 0.04	2.06	1.7 ± 0.2
Yb	0.1	0.3	0.00869	1.23 ± 0.06	1.1 ± 0.24	1.2 ± 0.04	1.3 ± 0.03	1.26 ± 0.06	1.29 ± 0.38	14.1	12 ± 0.4
Lu	0.1	0.5	0.00867	0.19 ± 0.02	0.2 ± 0.04	0.18 ± 0.02	0.204 ± 0.009	0.2 ± 0.01	0.19 ± 0.06	2.02	1.9 ± 0.1

<sup>a</sup> Average blank (1 mL 6 M HNO<sub>3</sub>) level of 15 pretreatment experiments.

<sup>b</sup> Average of 15 repeated analyses.

<sup>c</sup> Sediment diffusion coefficient at 25 °C.

<sup>d</sup> Single measurement.

<sup>e</sup> Compiled from 13 studies, Geological and Environmental Reference Materials (2013).



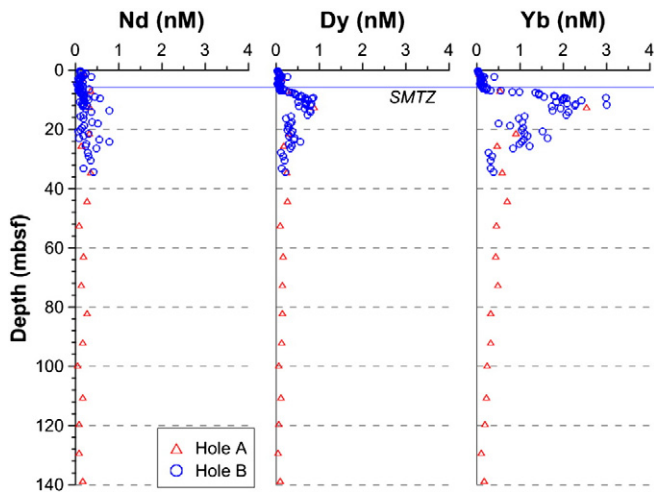


Fig. 4. Pore water concentration profiles of Nd, Dy and Yb representing LREE, MREE and HREE, respectively, for Holes A and B of Site U1345. The concentrations for the North Pacific Deep Water are Nd = 23.8 pM, Dy = 8.38 pM and Yb = 8.74 pM (Alibo and Nozaki, 1999).

## 4. Discussion

### 4.1. Paleo-environmental setting

The REE sources in the pore waters cannot be considered apart from the composition of the sedimentary column, and the latter is primarily controlled by climatic cycles and the associated changes in the sea level and shelf erosion. The age model for U1345 was constructed by Cook et al. (2011) based on the benthic foraminiferal  $\delta^{18}\text{O}$  stratigraphy. This age model assigns Peak 1 to the Holocene (~7 ka), Peak 2 to the end of MIS 3 (~30 ka) and the Shoulder to MIS 4 (~68 ka). According to the relative sea-level prediction for the Bering Strait (Hu et al., 2010), Peak 1 occurred when the sea-level was ~10 m lower than it is currently, Peak 2 occurred when the sea-level was ~80 m lower, and the Shoulder occurred when the sea-level was ~50 m lower. Both Peak 2 and the Shoulder are associated with sea level drops when the Bering Strait was closed or nearly so. Because the lower sea level suggests that more shelves were exposed, increased terrestrial input would have been likely. Currently, we do not have enough information regarding

the sedimentary composition for U1345 to support this claim, aside from the shipboard magnetic susceptibility data (Expedition 323 Scientists, 2011b). The magnetic susceptibility peaks were interpreted as terrestrial lithogenic material and coincided with the peaks in pore water REE (Fig. 10). At another Bering Slope site U1344, the delivery of coarser siliciclastic particles occurred mainly during the glacial periods, when diatom fluxes toward the sediment were lower (Aiello and Ravelo, 2012). On the Shirshov Ridge (Fig. 1), cold intervals including MIS 2–4 were characterized by high terrigenous matter supply (Riethdorf et al., 2013). It is likely that during these cold intervals oxic bottom water conditions were sustained due to active ventilation by sea ice formation and brine rejection. Oxic benthic foraminifera species were dominant during MIS 2 and 3 in a piston core collected very close to U1345 (core PC23A) (Kim et al., 2011).

### 4.2. Potential sources of dissolved REE in pore water

According to the pore water concentration profiles and the reaction rate modeling, dissolved REE was added to the pore waters at two depth intervals. At 1–3 mbsf, all REEs were produced (Fig. 5). Compared to the other intervals, especially the main production zone, the PAAS-normalized REE pattern for the 1–3 mbsf section was rather flat. As Peak 1 coincides with that of Mn but not Fe (Fig. 2), the reductive dissolution of Mn-oxides concomitantly released any associated REE (R1). Hydrogenous Mn-oxides have negatively charged surfaces at the pH of seawater and efficiently scavenge LREE-enriched mono-carbonate complexes ( $\text{LREE}(\text{CO}_3)^+$ ) from seawater (Ohta and Kawabe, 2001; Surya Prakash et al., 2012). Therefore, their eventual reduction in the sediment column would enrich the pore waters in LREE, explaining the relatively flat REE pattern in the 1–3 mbsf production zone (Fig. 7). A few of the uppermost samples in the production zone displayed a slight MREE bulge. In the upper 1–3 mbsf there was significant organic carbon degradation, as evidenced by the rapidly increasing alkalinity, DIC,  $\text{NH}_4^+$  and phosphate (Fig. 2); organic matter may add dissolved REEs to the pore waters (R1 and R2). POC scavenges REEs in the water column (Sholkovitz et al., 1994; Alibo and Nozaki, 1999), and the dissolved organic matter that forms during the degradation process within the sediments could complex the REE and generate a MREE-bulge pattern in the dissolved load (Pourret et al., 2007a; Pourret et al., 2007b; Tang and Johannesson, 2010). The relatively smaller peak size of the Mn compared to the 8–12 mbsf interval and the absence of the iron oxide reduction in this interval is interesting; it may be

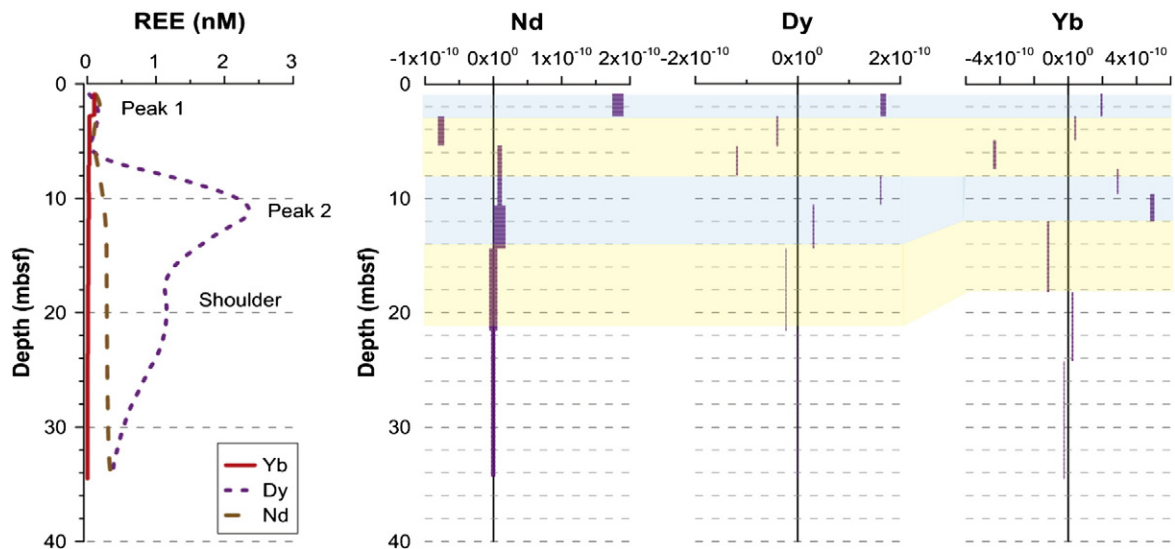
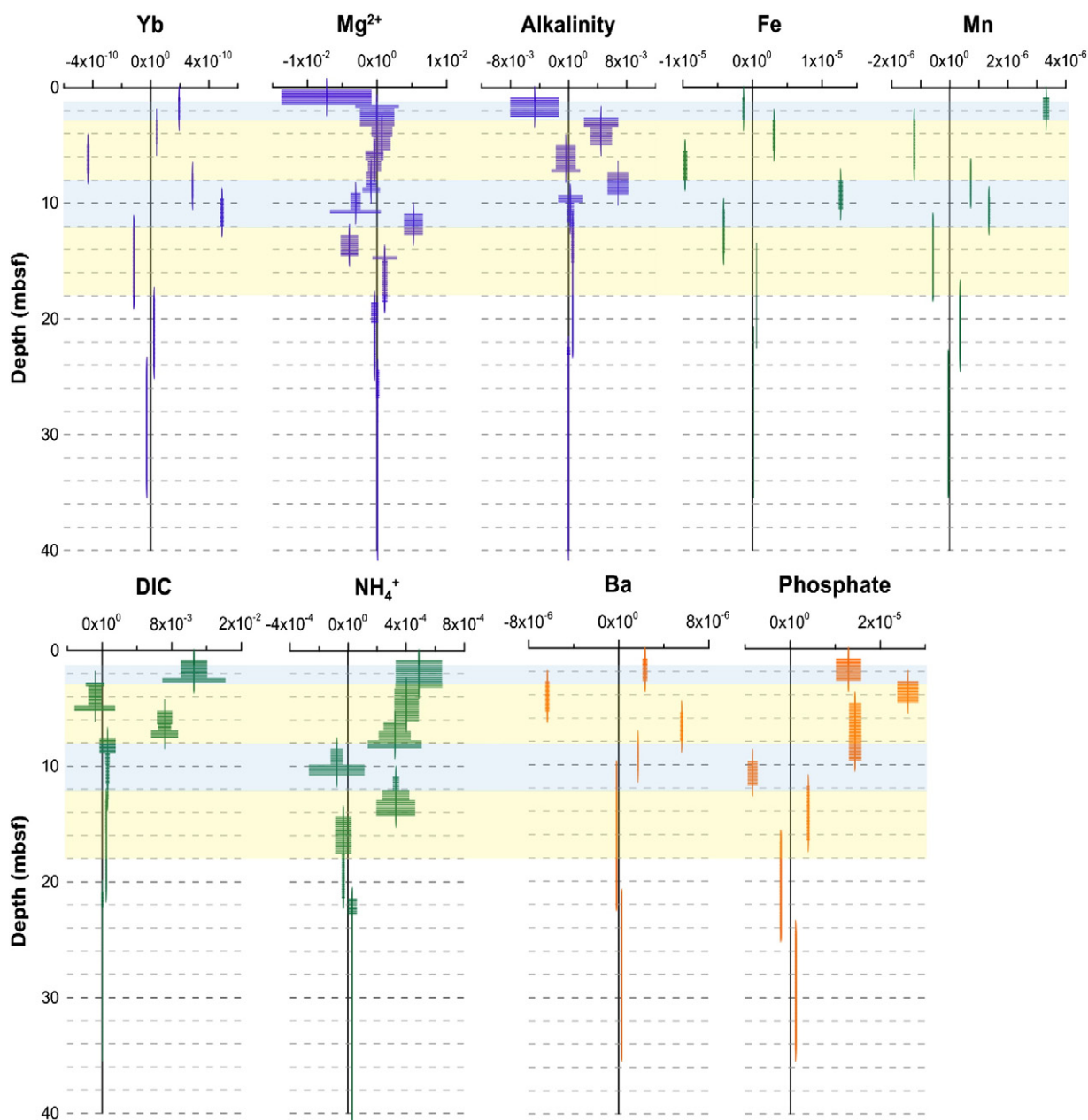


Fig. 5. Interpolated pore water concentration profiles and calculated reaction rates (in  $\text{mol m}^{-3} \text{y}^{-1}$ ) of the model (Wang et al., 2008) for Nd, Dy and Yb for the upper 40 mbsf. Positive values indicate production and negative values consumption. The uncertainties in reaction rates (horizontal error bars) are estimated by Monte Carlo assuming 10% analytical error. Different production and consumption zones are shaded.



**Fig. 6.** Production and consumption rates (in  $\text{mol m}^{-3} \text{y}^{-1}$ ) for Fe, Mn,  $\text{Mg}^{2+}$ , DIC,  $\text{NH}_4^+$ , Ba and phosphate based on pore water concentrations. Horizontal error bars indicate uncertainties in reaction rates. Different production and consumption zones of Yb are shaded.

because the site is currently located in an oxygen minimum zone and the Fe, Mn-oxyhydroxide phases were dissolved within the oxygen-depleted water column.

At 8–12 mbsf, there was significant production, especially for the HREE (Fig. 5). Both Fe and Mn were produced in this interval, but the magnitude was greater for Fe (Fig. 6). The peak Fe and Mn concentrations were  $19 \mu\text{M}$  and  $4.6 \mu\text{M}$ , respectively, and were three orders of magnitude higher than the peak HREE concentrations (2.3 nM range). The magnetic susceptibility was also high in this interval, coinciding with the REE, Fe and Mn peaks, which suggests that the dissolution of iron-containing minerals with high magnetic susceptibility was responsible (Fig. 10) in addition to a minor contribution from the Mn minerals. The most common iron mineral in the subsurface marine sediments is Fe-oxyhydroxide. Hydrogenous Fe-oxyhydroxide surfaces are neutral to slightly positively charged at the pH of seawater and scavenge HREE-enriched dicarbonate species ( $\text{HREE}(\text{CO}_3)_2^-$ ) (Ohta and Kawabe,

2001; Surya Prakash et al., 2012). Therefore, the reductive dissolution of Fe-oxyhydroxides would release HREE-enriched dissolved REE into pore waters (R5, R6 and R8). The organic carbon remineralization was not as significant at these depths as they were at the SMTZ and was no longer a major REE source. These results are supported by the decreased slopes in the alkalinity, DIC and  $\text{NH}_4^+$  profiles; these species are the best indicators for organic matter degradation (Fig. 2). Furthermore, the MREE-bulge pattern characteristic of complexation by natural dissolved organic matter was not observed at these depths (~8–12 m); a HREE-enrichment pattern was apparent instead.

The intense peak for the dissolved Fe and Mn below the SMTZ is rather unusual considering the standard diagenetic sequence: oxic respiration, nitrate/Mn reduction, Fe reduction, sulfate reduction and methanogenesis (Canfield and Thamdrup, 2009). When this sediment interval was deposited, the environmental conditions were different from today. Delivery of terrigenous material was higher to this site,

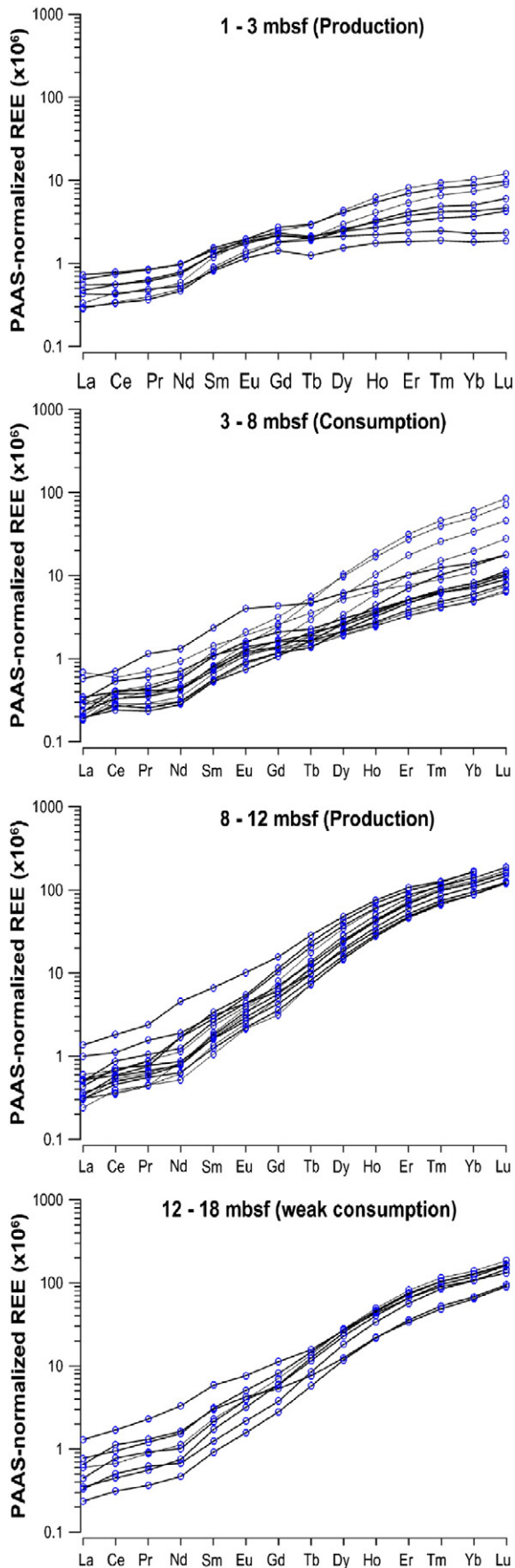


Fig. 7. Shale-normalized REE pattern in the pore waters for the different production-consumption intervals.

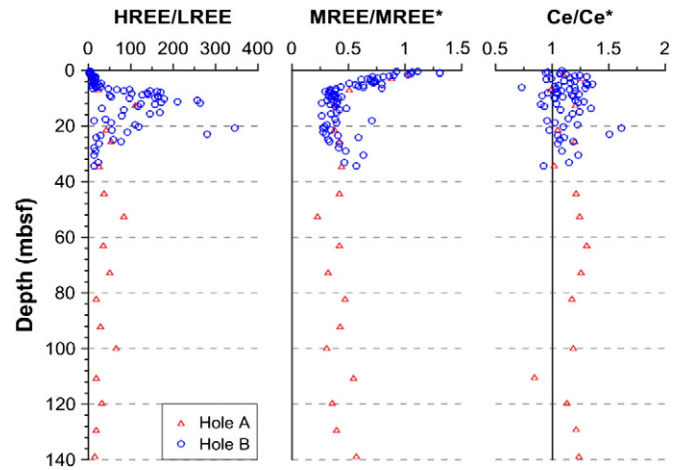


Fig. 8. Depth profiles of parameters showing the REE pattern in the pore waters: the  $Yb_n/Nd_n$  ratio representing HREE/LREE, the  $MREE/MREE^* = 2Dy_n/(Nd_n + Yb_n)$  proxy for the MREE bulge and the  $Ce/Ce^* = Ce_n/(2Pr_n - Nd_n)$  indicating the Ce anomaly. All REE concentrations are shale-normalized (subscripted n).

and what was delivered largely escaped reductive dissolution in the water column as the bottom waters were oxic. Due to the rapid sedimentation rate at this site ( $\sim 300$  m/Myr), the Fe–Mn oxyhydroxides were quickly buried below the SMTZ and largely preserved. Utilizing the approach used by Pohlman et al. (2009), we estimated the average time that the 8–12 mbsf layer spent above the SMTZ as  $6 \text{ m}/(300 \text{ m/Myr}) = 20 \text{ kyr}$ .

As an alternative source of REEs, as well as Fe and Mn, in the main production zone, we considered silicate weathering. Reactive silicate minerals in the sub-surface sediments may dissolve under anoxic conditions (Wallmann et al., 2008; Scholz et al., 2013). Volcanic settings, in particular, provide reactive glass and minerals, such as olivines and pyroxenes. Pyroxenes contain significant amounts of REE, while being generally enriched in HREE due to higher compatibility (Olin and Wolff, 2010). Especially high REE concentrations were observed in the pore waters of volcanic ash layers with low rates of anaerobic organic degradation (Schacht et al., 2010). At Site U1345, thin ash layers were observed at 1.4–1.6 mbsf for Holes A and C as well as for 107.2–107.3 mbsf for Hole C (Expedition 323 Scientists, 2011b); however, increased REE concentrations were not apparent in the pore water samples near those depths. Among the Bering Sea IODP Exp. 323 sites, volcanic ash was higher in the Bowers Ridge cores closer to the Aleutian Islands and diminished toward the Bering Slope (Aiello and Ravelo, 2012). A provenance study using Sr and Nd isotopes on the detritus of surface sediments proximal to Site U1345 suggested that on a mixing line between the Aleutian Arc and Yukon River sources, the sediments were close to the Yukon River endmember (Asahara et al., 2012). Nevertheless, there are various sources of volcanogenic material surrounding the Bering Sea, e.g. the Okhotsk–Chutkoka Volcanic Belt, Kamchatka Arc and Aleutian Arc, and the importance of each input to site U1345 may have varied in time.

While we lack detailed information regarding the sedimentary composition at U1345, we may use the pore water's Mg and alkalinity profiles to search for potential silicate weathering markers. While the Ca variations in pore water may be dominated by precipitation of authigenic carbonates, Mg is less affected and is an element common in volcanic minerals. Silica may not be a good proxy because  $Si(OH)_4$  released during weathering of primary silicates can be almost completely bound in cation-poor authigenic silicates (Wallmann et al., 2008). The Mg enrichment from 8 to 36 mbsf at Site U1345 (Fig. 2) may be due to dissolution of Mg-bearing silicate phases. The alkalinity reached a plateau of  $\sim 50$  mM (Expedition 323 Scientists, 2011b). In this interval, the Ca concentrations decreased, suggesting that the actual alkalinity production was even larger but that it was consumed during



**Table 5**Calculated REE flux across the sediment–water interface ( $\text{nmol m}^{-2} \text{y}^{-1}$ ). PAAS and NPDW compositions are listed.

REE	Bering Sea Slope <sup>a</sup>	Cascadia margin <sup>b</sup>	California margin 8 <sup>c</sup>	California margin 9 <sup>c</sup>	California margin 10 <sup>c</sup>	Nazca Ridge <sup>c</sup>	Buzzards Bay 1 <sup>d</sup>	Buzzards Bay 2 <sup>e</sup>	Niger Delta 1 <sup>f</sup>	Niger Delta 2 <sup>f</sup>	PAAS (ppm) <sup>g</sup>	NPDW (pM) <sup>h</sup>
Y	0.28	–	–	–	–	–	–	–	–	–	38.2	38.7
La	0.08	0.04	35	19	32	12	1.3	0.32	5.4	13	38.2	38.7
Ce	0.29	0.12	67	35	54	3.0	6.4	7.3	19	39	79.6	3.98
Pr	0.03	0.01	7.3	3.5	8.8	2.8	–	–	2.1	3.5	8.83	5.1
Nd	0.11	0.05	29	18	37	11	1.2	1.2	8.3	13	33.9	23.8
Sm	0.03	0.02	5.8	3.2	7.8	2.8	0.28	0.36	1.5	2.5	5.55	4.51
Eu	0.01	0.005	1.2	0.77	1.9	0.74	0.06	0.08	0.29	0.57	1.08	1.24
Gd	0.03	0.03	6.1	3.7	6.0	4.0	0.25	–	1.1	1.9	4.66	6.83
Tb	0.005	0.005	0.84	0.60	1.4	0.73	–	–	0.18	0.25	0.774	1.13
Dy	0.03	0.04	4.8	2.7	9.0	5.3	–	0.59	1.1	1.3	4.68	8.38
Ho	0.01	0.01	0.82	0.61	1.5	1.1	–	–	0.22	0.23	0.991	2.34
Er	0.02	0.05	2.6	1.8	5.5	4.1	–	0.52	0.64	0.59	2.85	7.94
Tm	0.003	0.01	0.35	0.35	0.8	0.80	–	–	–	–	0.405	1.23
Yb	0.02	0.08	2.0	2.3	4.4	5.9	–	0.58	0.48	0.53	2.82	8.74
Lu	0.004	0.02	0.24	0.44	0.9	1.3	–	–	0.06	0.08	0.433	1.46

<sup>a</sup> This study.<sup>b</sup> Kim et al. (2012).<sup>c</sup> Haley et al. (2004).<sup>d</sup> Sholkovitz et al. (1989).<sup>e</sup> Elderfield and Sholkovitz (1987), re-calculated.<sup>f</sup> Bayon et al. (2011b).<sup>g</sup> Taylor and McLennan (1995).<sup>h</sup> Alibo and Nozaki (1999).

precipitation of authigenic carbonates. A simple account of the alkalinity budget may be useful (Scholz et al., 2013). Because the sulfate concentration profile was nearly linear, the sulfate reduction coupled with AOM (R3) accounts for most of the sulfate consumption; the organoclastic sulfate reduction (R2) was only minor. Iron and Mn reductions yielded only a sub-mEq of alkalinity (R1, R5). During methanogenesis,  $\text{CO}_2$  was produced but did not increase carbonate alkalinity. According to the stoichiometry of R2 and using the seawater sulfate concentration of ~28 mM, alkalinity produced during the early diagenesis of organic matter is less than 60 mM. Therefore, alkalinity values greater than 60 mM would suggest that other sources, perhaps silicate weathering, is responsible. However, in our core, the alkalinity is less than 50 mEq in the upper 40 mbsf; we think that silicate weathering is minor.

Diatoms also have been proposed as REE sources as they carry REE adsorbed on their shells (Akagi et al., 2011). However, it is difficult to explain a sudden diagenesis of opal in the two depth intervals when pH and alkalinity varied smoothly with depth. The dissolved silica concentrations were scattered in the upper 40 mbsf (Expedition 323 Scientists, 2011b).

In addition to mineralogy, physico-chemical parameters also may play a role in determining the overall REE pattern in the pore water. The pore water chemistry governs the relative amount of inorganic carbonate versus the dissolved organic compounds (acetate, formate, humic acids) that could complex with the REEs (Rongemaille et al., 2011). For the carbonates, complexes containing HREEs are more thermodynamically stable than those with LREEs (Cantrell and Byrne, 1987; Byrne and Kim, 1990; Byrne and Kim, 1993; Lee and Byrne, 1993). In the SMTZ, the alkalinity reached high values due to significant  $\text{HCO}_3^-$  and  $\text{HS}^-$  release into the pore waters (R3). This high alkalinity may lead to the HREE-enriched patterns consistent with previous studies (Rongemaille et al., 2011). In the pore waters' pH range (7.5–7.9), humic and fulvic acids are important complexing agents, which would yield a rather flat REE pattern with a slight MREE-bulge

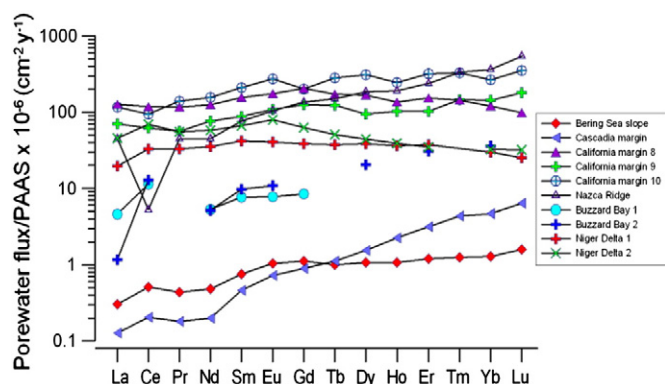


**Fig. 9.** REE fluxes across the sediment–water interface for diverse geographic locations where pore water data exist. See Table 5 for references.

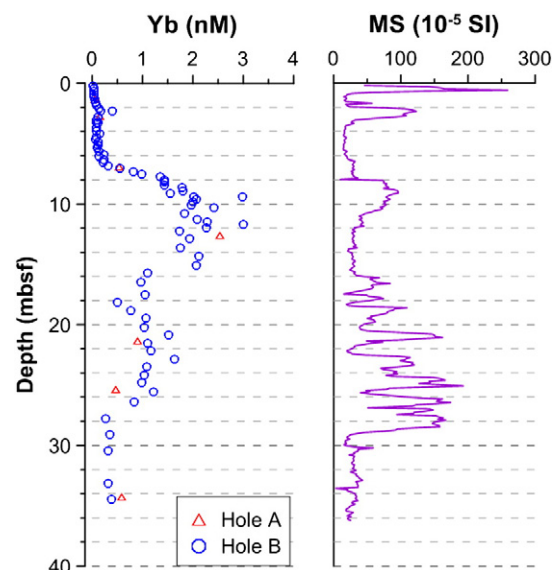


**Fig. 10.** Shipboard measurements of magnetic susceptibility (MS) for Hole B (Expedition 323 Scientists, 2011b).



(Pourret et al., 2007a; Pourret et al., 2007b). Because we do not have data for organics that are dissolved or coating the solid phase, we can only draw conclusions based on alkalinity levels and REE patterns. From the high alkalinity values and the HREE-enriched pattern, we expect that carbonate complexation rather than humic acid complexation is dominant.

Below approximately 25 mbsf, there was no change in the pore water REE contents and no production or consumption, most likely due to a lack of appropriate microbial reactions and reactive labile components in the sediment. Deeper variations in pore water REEs have been reported to be associated with the alteration of discrete ash layers (Schacht et al., 2010) or deep fluid migration (Kim et al., 2012); however, no evidence of either was present for site U1345 at the resolution in which the pore water was sampled.

#### 4.3. Potential sinks for dissolved REE from pore water

According to the reaction rate model, two depth intervals were sinks for the REEs from pore waters: at 3–8 mbsf and, less significantly, at 12–18 mbsf. We evaluated the potential mineral phases that could incorporate REEs and act as sinks based on the pore water concentrations of constituent species and the REE patterns: carbonate, apatite, reduced iron minerals, barite and clay minerals.

The precipitation of Mg-rich calcite or dolomite at the SMTZ (6.3 mbsf) (Wehrmann et al., 2011) could incorporate REEs (Banner et al., 1988); the REE pattern in aragonite and calcite reflects that of the water from which it precipitated and does not display any fractionation during precipitation (Terakado and Masuda, 1988). Consistent with this, there was little change in the general REE pattern between the main production zone (8–12 mbsf) and the two sink zones above and below it.

Carbonate fluorapatite (CFA) scavenges REEs (Shaw and Wasserburg, 1985; Martin and Haley, 2000), and REEs coprecipitate with CFA (Byrne and Kim, 1993; Rasmussen et al., 1998); MREE preferentially adsorbs onto the CFA (Takebe, 2005; Takebe and Yamamoto, 2007). In our pore water profiles, there was not any noticeable MREE depletion, and the REE consumption depth intervals (3–8 and 12–18 mbsf) did not coincide with those of phosphate (10–12 mbsf). Therefore, we do not think CFA was a major REE sink at this site.

The reduced Fe phase (carbonate, sulfide) is another potential sink. Generally, coupled sulfate reduction and iron oxyhydroxide dissolution can precipitate iron sulfides or carbonates (Jørgensen and Kasten, 2006). The total  $H_2S$  peak at the SMTZ (Fig. 2) suggests that reactive iron oxyhydroxides are not abundant enough in this interval for iron sulfide minerals to consume all the  $H_2S$ . However, the frequent occurrence of pyrite mottles and specks suggests that this is a viable REE sink (Chaillou et al., 2006). High REE contents were observed for siderites ( $FeCO_3$ ) at cold seeps, and the REE patterns reflected the fluid source (Rongemaille et al., 2011). Although siderites are thermodynamically unstable under even trace amounts of dissolved sulfide, below the SMTZ, if reactive iron is present and if the Fe/Ca ratio is high enough, siderite may precipitate (Haese, 2006).

Precipitation of barite may also scavenge REEs (Guichard et al., 1979; Martin et al., 1995). Because the Bering Sea Slope has high biological productivity, biogenic barite is expected. The deep pore waters have high concentrations of dissolved Ba, most likely due to the diagenetic remobilization of biogenic barite in the sulfate depleted pore waters (Von Breymann et al., 1992); the dissolved Ba may be consumed just above the SMTZ as authigenic barite, causing the pore water Ba concentrations to drop (Figs. 2, 6). This process cannot explain the deeper sink zone due to the lack of sulfate.

Clay minerals (kaolinite, smectite, chlorite, illite–montmorillonite) have also been proposed as potential REE sinks that prefer LREEs over HREEs (Coppin et al., 2002). However, the humic coatings, rather than clays themselves, may be the major agents that complex and adsorb REEs (Wan and Liu, 2006).

In summary, the Mg-rich carbonate, iron sulfide and barite may be responsible for the principal (3–8 mbsf) sink zone, and siderite for the deeper (12–18 mbsf) sink zone.

#### 4.4. Pore water REE patterns and fluxes

The pore water profiles were analyzed on the Bering Sea Slope down to 140 mbsf, and comparisons with the literature data from around the world revealed a large spatial variability in the vertical REE production/consumption and sediment-to-seawater fluxes. Within the pore water profile, there was a major production zone below the SMTZ. The magnitude was especially large for the HREE and was most likely due to the reductive dissolution of iron oxyhydroxides or silicate weathering of ferromagnesian minerals. This feature is characteristic for this region; in other parts of the world, the same feature may not be observed. At the Bering Sea Slope, the substrate was rich in Fe minerals that had escaped dissolution during early diagenesis, most likely due to rapid burial of the abundant terrigenous matter under oxic bottom water conditions. Spatially, there were also large variations in the diffusive fluxes from the pore waters of the subsurface sediments to the deep waters. There are some uncertainties in this calculation because the depth interval varies across different studies due to different sampling depth resolutions. Regardless, anoxic basins or those with cold seeps exhibited higher fluxes than the Bering Sea Slope. The REE patterns also varied between the sites. At our site, we mainly observed HREE-enriched patterns, except at the upper ~2 mbsf. In the literature, there have been reports of pronounced MREE-bulge patterns in anoxic basins, albeit at much shallower depths, as reported by Haley et al. (2004).

### 5. Conclusions

The REEs were investigated in pore water samples from two sediment cores drilled down to ~140 mbsf at the IODP U1345 site on the Bering Sea Slope. The REE concentrations in the pore waters were enriched relative to the deep seawater, indicating that there was significant liberation from sediment during diagenesis. The NPDW-normalized pattern revealed a relatively constant, positive Ce anomaly (average  $Ce/Ce^* = 10.1 \pm 1.1$ , similar to PAAS: 9.8). Two significant fractionations within the REE series were observed in the sedimentary pore water profiles. First, the relatively flat pattern featuring MREE enrichment at shallow depths was most likely due to the reduction of LREE-enriched Mn oxides and the disintegration of MREE-enriched organic matter. Second, HREE enrichment was observed over most of the depth profile below ~1 mbsf, including a HREE peak (8–12 mbsf) and shoulder (18–24 mbsf). The sources of the REE at those depths were likely reactive iron oxyhydroxides or ferromagnesian silicate minerals. The likely sinks for the REEs produced in the above zones include carbonate and perhaps some barite precipitation at 3–8 mbsf. Therefore, the precipitation of authigenic minerals related to the anaerobic oxidation of methane in sediments may represent a net sink for REE. The upward diffusion fluxes for REEs at the sediment/water interface were calculated for sites with existing pore water data, and a large range was observed. The values for the Bering Sea Slope were lower, reflecting the flux over longer depth scales relative to the other sites.

### Acknowledgments

This research used samples and data provided by the Integrated Ocean Drilling Program (IODP). This research was part of the project titled “Integrated Ocean Drilling Program” funded by the Ministry of Land, Transport and Maritime Affairs, Korea. The authors would like to thank the SNU-NCIRF for the access to the instrumentation as well as L. Wehrmann, C. Marz, Nils Risgaard-Petersen, H. Schrumm and M. Cook for the discussions. The comments from G. Bayon and an anonymous reviewer greatly improved this paper.

## References

- Aiello, I.W., Ravelo, A.C., 2012. Evolution of marine sedimentation in the Bering Sea since the Pliocene. *Geosphere* 8 (6). <http://dx.doi.org/10.1130/GES00710.1>.
- Akagi, T., Fu, F.-f., Hongbo, Y., Takahashi, K., 2011. Composition of rare earth elements in settling particles collected in the highly productive North Pacific Ocean and Bering Sea: implications for siliceous-matter dissolution kinetics and formation of two REE-enriched phases. *Geochim. Cosmochim. Acta* 75, 4857–4876.
- Alibo, D.S., Nozaki, Y., 1999. Rare earth elements in seawater: particle association, shale-normalization, and Ce oxidation. *Geochim. Cosmochim. Acta* 63 (3–4), 363–372.
- Asahara, Y., Takeuchi, F., Nagashima, K., Harada, N., Yamamoto, K., Oguri, K., Tadai, O., 2012. Provenance of terrigenous detritus of the surface sediments in the Bering and Chukchi Seas as derived from Sr and Nd isotopes: implications for recent climate change in the Arctic regions. *Deep Sea Res. Part II* 61–64, 155–171.
- Banner, J.L., Hanson, G.N., Meyers, W.J., 1988. Rare earth element and Nd isotopic variations in regionally extensive dolomites from the Burlington–Keokuk Formation (Mississippian); implications for REE mobility during carbonate diagenesis. *J. Sed. Res.* 58, 415–432.
- Bayon, G., Birot, D., Bollinger, C., Barrat, J.A., 2011a. Multi-element determination of trace elements in natural water reference materials by ICP-SFMS after Tm addition and iron co-precipitation. *Geostand. Geoanal. Res.* 35 (1), 145–153.
- Bayon, G., Birot, D., Ruffine, L., Caprais, J.-C., Ponzevera, E., Bollinger, C., Donval, J.-P., Charlou, J.-L., Voisset, M., Grimaud, S., 2011b. Evidence for intense REE scavenging at cold seeps from the Niger Delta margin. *Earth Planet. Sci. Lett.* 312, 443–452.
- Berner, R.A., 1980. *Early Diagenesis: A Theoretical Approach*. Princeton University Press, Princeton, New Jersey (241 pp.).
- Boudreau, B.P., 1997. *Diagenetic Models and Their Implementation: Modelling Transport and Reactions in Aquatic Sediments*. Springer-Verlag, Berlin.
- Byrne, R.H., Kim, K.-H., 1990. Rare earth element scavenging in seawater. *Geochim. Cosmochim. Acta* 54, 2645–2656.
- Byrne, R.H., Kim, K.-H., 1993. Rare earth precipitation and coprecipitation behavior: the limiting role of  $\text{PO}_4^{3-}$  on dissolved rare earth concentrations in seawater. *Geochim. Cosmochim. Acta* 57 (3), 519–526.
- Canfield, D.E., Thamdrup, B., 2009. Toward a consistent classification scheme for geochemical environments, or, why we wish the term 'suboxic' would go away. *Geobiology* 7, 385–392.
- Canfield, D.E., Thamdrup, B., Hansen, J.W., 1993. The anaerobic degradation of organic matter in Danish coastal sediments: iron reduction, manganese reduction, and sulfate reduction. *Geochim. Cosmochim. Acta* 57, 3867–3883.
- Cantrell, K.J., Byrne, R.H., 1987. Rare earth element complexation by carbonate and oxalate ions. *Geochim. Cosmochim. Acta* 51 (3), 597–605.
- Chaillou, G., Anschutz, P., Lavaux, G., Blanc, G., 2006. Rare earth elements in the modern sediments of the Bay of Biscay (France). *Mar. Chem.* 100, 39–52.
- Cook, M.S., Mix, A., Ravelo, C., 2011. The benthic oxygen isotope stratigraphy from U1339 and U1345, Integrated Ocean Drilling Program Postcruise Meeting, Salamanca, Spain.
- Coppin, F., Berger, G., Bauer, A., Castet, S., Loubet, M., 2002. Sorption of lanthanides on smectite and kaolinite. *Chem. Geol.* 182, 57–68.
- Elderfield, H., Sholkovitz, E.R., 1987. Rare earth elements in the pore waters of reducing nearshore sediments. *Earth Planet. Sci. Lett.* 82, 280–288.
- Esser, B.K., Volpe, A., Kenneally, J.M., Smith, D.C., 1994. Preconcentration and purification of rare earth elements in natural waters using silica-immobilized 8-hydroxyquinoline and a supported organophosphorus extractant. *Anal. Chem.* 66, 1736–1742.
- Expedition 323 Scientists, 2011a. Methods. In: Takahashi, K., Ravelo, A.C., Alvarez Zarikian, C.A., the Expedition 323 Scientists (Eds.), *Proc. IODP, 323. Integrated Ocean Drilling Program Management International, Inc.*, Tokyo.
- Expedition 323 Scientists, 2011b. Site U1345. In: Takahashi, K., Ravelo, A.C., Alvarez Zarikian, C.A., the Expedition 323 Scientists (Eds.), *Proc. IODP, 323. Integrated Ocean Drilling Program Management International, Inc.*, Tokyo.
- Freslon, N., Bayon, G., Birot, D., Bollinger, C., Barrat, J.A., 2011. Determination of rare earth elements and other trace elements (Y, Mn, Co, Cr) in seawater using Tm addition and  $\text{Mg}(\text{OH})_2$  co-precipitation. *Talanta* 85, 582–587.
- Geological and Environmental Reference Materials, 2013. <http://georem.mphc-mainz.gwdg.de/>.
- German, C.R., Elderfield, H., 1989. Rare earth elements in Saanich Inlet, British Columbia, a seasonally anoxic basin. *Geochim. Cosmochim. Acta* 53, 2561–2571.
- Gieskes, J.M., Gamo, T., Brumsack, H., 1991. Chemical methods for interstitial water analysis aboard JOIDES Resolution. *ODP Tech. Note*, 15. <http://dx.doi.org/10.2973/odp.tn.15.1991>.
- Guichard, F., Church, T.M., Treuil, M., Jaffrezic, H., 1979. Rare earths in barites: distribution and effects on aqueous partitioning. *Geochim. Cosmochim. Acta* 43, 983–997.
- Haese, R.R., 2006. The biogeochemistry of iron. In: Schulz, H.D., Zabel, M. (Eds.), *Marine Geochemistry*. Springer-Verlag, Berlin, pp. 241–270.
- Haley, B.A., Klinkhammer, G.P., McManus, J., 2004. Rare earth elements in pore waters of marine sediments. *Geochim. Cosmochim. Acta* 68 (6), 1265–1279.
- Hu, A., Meehl, G.A., Otto-Bliesner, B.L., Waelbroeck, C., Han, W., Loutre, M.-F., Lambeck, K., Mitrovica, J.X., Rosenbloom, N., 2010. Influence of Bering Strait flow and North Atlantic circulation on glacial sea-level changes. *Nat. Geosci.* <http://dx.doi.org/10.1038/ngo729>.
- Hurst, M.P., Aguilar-Isas, A.M., Bruland, K.W., 2010. Iron in the southeastern Bering Sea: elevated leachable particulate Fe in shelf bottom waters as an important source for surface waters. *Cont. Shelf Res.* 30, 467–480.
- Jørgensen, B.B., Kasten, S., 2006. Sulfur cycling and methane oxidation. In: Schulz, H.D., Zabel, M. (Eds.), *Marine Geochemistry*. Springer-Verlag, Berlin, pp. 271–309.
- Kim, S., Khim, B.K., Uchida, M., Itaki, T., Tada, R., 2011. Millennial-scale paleoceanographic events and implication for the intermediate-water ventilation in the northern slope area of the Bering Sea during the last 71 kyrs. *Global Planet. Change* 79, 89–98.
- Kim, J.-H., Torres, M.E., Haley, B.A., Kastner, M., Pohlman, J.W., Riedel, M., Lee, Y.-J., 2012. The effect of diagenesis and fluid migration on rare earth element distribution in pore fluids of the northern Cascadia accretionary margin. *Chem. Geol.* 291, 152–165.
- Lawrence, M.G., Kamber, B.S., 2007. Rare earth element concentrations in the natural water reference materials (NRCC) NASS-5, CASS-4 and SLEW-3. *Geostand. Geoanal. Res.* 31 (2), 95–103.
- Lee, J.H., Byrne, R.H., 1993. Complexation of trivalent rare earth elements (Ce, Eu, Gd, Tb, Yb) by carbonate ions. *Geochim. Cosmochim. Acta* 57 (2), 295–302.
- Li, Y.-H., Gregory, S., 1974. Diffusion of ions in sea water and in deep-sea sediments. *Geochim. Cosmochim. Acta* 38 (5), 703–714.
- Manheim, F.T., Brooks, E.G., Winters, W.J., 1994. Description of a hydraulic sediment squeezer. *U.S. Geol. Surv. Open-File Report*, 94–584.
- Martin, E.E., Haley, B.A., 2000. Fossil fish teeth as proxies for seawater Sr and Nd isotopes. *Geochim. Cosmochim. Acta* 64, 835–847.
- Martin, E.E., MacDougall, J.D., Herbert, T.D., Paytan, A., Kastner, M., 1995. Strontium and neodymium analyses of marine barite separates. *Geochim. Cosmochim. Acta* 59, 1353–1361.
- Mix, A.C., Tiedemann, R., Blum, P., Abrantes, F.F., Benway, H., Cacho-Lascorz, I., Chen, M.-T., Delaney, M.L., Flores, J.-A., Giosan, L., Holbourn, A.E., Irino, T., Iwai, M., Joseph, L.H., Kleiven, H.F., Lamy, F., Lund, S.P., Martinez, P., McManus, J.F., Ninnemann, U.S., Pisias, N.G., Robinson, R.S., Stoner, J.S., Sturm, A., Wara, M.W., Wei, W., 2003. Proceedings of the Ocean Drilling Program 202. <http://dx.doi.org/10.2073/opd.proc.ir.202.2003> (Initial Reports, pp.).
- Murray, R.W., Miller, D.J., Kryc, K.A., 2000. Analysis of major and trace elements in rocks, sediments, and interstitial waters by inductively coupled plasma-atomic emission spectrometry (ICP-AES). *ODP Tech. Note*, 29. <http://dx.doi.org/10.2973/odp.tn.29.2000>.
- Nozaki, Y., 2001. Rare earth elements and their isotopes in the ocean. In: Steele, J.H., Turekian, K.K., Thorpe, S.A. (Eds.), *Marine Chemistry and Geochemistry*. Academic Press, pp. 653–665.
- Ohta, A., Kawabe, I., 2001. REE(III) adsorption onto Mn dioxide ( $\delta\text{-MnO}_2$ ) and Fe oxyhydroxide: Ce(III) oxidation by  $\delta\text{-MnO}_2$ . *Geochim. Cosmochim. Acta* 65 (5), 695–703.
- Olin, P.H., Wolff, J.A., 2010. Rare earth and high field strength element partitioning between iron-rich clinopyroxenes and felsic liquids. *Contrib. Mineral. Petrol.* 160, 761–775.
- Pohlman, J.W., Kaneko, M., Heuer, V.B., Coffin, R.B., Whiticar, M., 2009. Methane sources and production in the northern Cascadia margin gas hydrate system. *Earth Planet. Sci. Lett.* 287, 504–512.
- Pourret, O., Davranche, M., Gruau, G., Dia, A., 2007a. Competition between humic acid and carbonates for rare earth elements complexation. *J. Colloid Interface Sci.* 305, 25–31.
- Pourret, O., Davranche, M., Gruau, G., Dia, A., 2007b. Rare earth elements complexation with humic acid. *Chem. Geol.* 243, 128–141.
- Rasmussen, B., Buick, R., Taylor, W., 1998. Removal of oceanic REE by authigenic precipitation of phosphatic minerals. *Earth Planet. Sci. Lett.* 164, 135–149.
- Riethdorf, J.-R., Nürnberg, D., Max, L., Tiedemann, R., Gorbarenko, S.A., Malakhov, M.I., 2013. Millennial-scale variability of marine productivity and terrigenous matter supply in the western Bering Sea over the past 180 kyr. *Clim. Past* 9, 1345–1373.
- Rongemille, E., Bayon, G., Pierre, C., Bollinger, C., Chu, N.C., Fouquet, Y., Riboulot, V., Voisset, M., 2011. Rare earth elements in cold seep carbonates from the Niger delta. *Chem. Geol.* 286, 196–206.
- Sambrotto, R.N., Mordy, C., Zeeman, S.I., Stabeno, P.J., Macklin, S.A., 2008. Physical forcing and nutrient conditions associated with patterns of Chl a and phytoplankton productivity in the southeastern Bering Sea during summer. *Deep Sea Res. Part II* 55, 1745–1760.
- Schacht, U., Wallmann, K., Kutterolf, S., 2010. The influence of volcanic ash alteration on the REE composition of marine pore waters. *J. Geochem. Explor.* 106, 176–187.
- Scholz, F., Hensen, C., Schmidt, M., Geersen, J., 2013. Submarine weathering of silicate minerals and the extent of pore water freshening at active continental margins. *Geochim. Cosmochim. Acta* 100, 200–216.
- Shaw, H.F., Wasserburg, G.J., 1985. Sm–Nd in marine carbonates and phosphates: implications for Nd isotopes in seawater and crustal ages. *Geochim. Cosmochim. Acta* 49, 503–518.
- Shaw, T.J., Duncan, T., Schnetger, B., 2003. A preconcentration/matrix reduction method for the analysis of rare earth elements in seawater and groundwaters by isotope dilution ICPMS. *Anal. Chem.* 75, 3396–3403.
- Shimizu, H., Tachikawa, K., Masuda, A., Nozaki, Y., 1994. Cerium and neodymium isotope ratios and REE patterns in seawater from the North Pacific Ocean. *Geochim. Cosmochim. Acta* 58, 323–333.
- Sholkovitz, E., Elderfield, H., 1988. Cycling of dissolved rare earth elements in Chesapeake Bay. *Global Biogeochem. Cycles* 2 (2), 157–176.
- Sholkovitz, E.R., Piepgras, D.J., Jacobsen, S.B., 1989. The pore water chemistry of rare earth elements in Buzzards Bay sediments. *Geochim. Cosmochim. Acta* 53, 2847–2856.
- Sholkovitz, E.R., Shaw, T.J., Schneider, D.L., 1992. The geochemistry of rare earth elements in the seasonally anoxic water column and porewaters of Chesapeake Bay. *Geochim. Cosmochim. Acta* 56, 3389–3402.
- Sholkovitz, E.R., Landing, W.M., Lewis, B.L., 1994. Ocean particle chemistry: the fractionation of rare earth elements between suspended particles and seawater. *Geochim. Cosmochim. Acta* 58 (6), 1567–1579.
- Soyol-Erdene, T.-O., Han, Y., Lee, B., Huh, Y., 2011. Sources and fluxes of Pt, Ir and REE in the Seoul metropolitan area through wet scavenging processes. *Atmos. Environ.* 45, 1970–1978.
- Springer, A.M., McRoy, C.P., Flint, M.V., 1996. The Bering Sea green belt: shelf-edge processes and ecosystem production. *Fish. Oceanogr.* 5 (3/4), 205–223.

- Surya Prakash, L., Ray, D., Paropkari, A.L., Mudholkar, A.V., Satyanarayanan, M., Sreenivas, B., Chandrasekharam, D., Kota, D., Kamesh Raju, K.A., Kaisary, S., Balaran, V., Gurav, T., 2012. Distribution of REEs and yttrium among major geochemical phases of marine Fe–Mn-oxides: comparative study between hydrogenous and hydrothermal deposits. *Chem. Geol.* 312–313, 127–137.
- Takahashi, K., 1999. Paleocceanographic changes and present environment of the Bering Sea. In: Loughlin, T.R., Ohtani, K. (Eds.), *Dynamics of the Bering Sea*. University of Alaska Sea Grant, Fairbanks, Alaska, pp. 365–385.
- Takahashi, K., Ravelo, A.C., Zarijian, C.A., Expedition, I.O.D.P., IODP Expedition 323 Scientists, 2011. IODP Expedition 323—Pliocene and Pleistocene paleocceanographic changes in the Bering Sea. *Sci. Drill.* 11, 4–13.
- Takebe, M., 2005. Carriers of rare earth elements in Pacific deep-sea sediments. *J. Geol.* 113, 201–215.
- Takebe, M., Yamamoto, K., 2007. Relative REE abundances of porewater in Pacific pelagic sediment: estimation by equilibrium calculations based on REE composition of Mn-oxide and apatite components. *Bull. Nagoya Univ. Mus.* 23, 1–12.
- Tang, J., Johannesson, K.H., 2010. Ligand extraction of rare earth elements from aquifer sediments: implications for rare earth element complexation with organic matter in natural waters. *Geochim. Cosmochim. Acta* 74, 6690–6705.
- Taylor, S.R., McLennan, S.M., 1995. The geochemical evolution of continental crust. *Rev. Geophys.* 33 (2), 241–265.
- Terakado, Y., Masuda, A., 1988. The coprecipitation of rare-earth elements with calcite and aragonite. *Chem. Geol.* 69, 103–110.
- Von Breyman, M.T., Brumsack, H., Emeis, K.C., 1992. Depositional and diagenetic behavior of barium in the Japan Sea. In: Pisciotto, K.A., Ingle Jr., J.C., von Breyman, M.T., Barron, J., et al. (Eds.), *Proceedings of the Ocean Drilling Program, Scientific Results*, pp. 651–665.
- Wallmann, K., Aloisi, G., Haeckel, M., Tishchenko, P., Pavlova, G., Greinert, J., Kutterolf, S., Eisenhauer, A., 2008. Silicate weathering in anoxic marine sediments. *Geochim. Cosmochim. Acta* 72, 3067–3090.
- Wan, Y., Liu, C., 2006. The effect of humic acid on the adsorption of REEs on kaolin. *Colloids Surf. A* 290, 112–117.
- Wang, G., Spivack, A.J., Rutherford, S., Manor, U., D'Hondt, S., 2008. Quantification of co-occurring reaction rates in deep subseafloor sediments. *Geochim. Cosmochim. Acta* 72 (14), 3479–3488.
- Wehrmann, L.M., Risgaard-Petersen, N., Schrum, H.N., Walsh, E.A., Huh, Y., Ikehara, M., Pierre, C., D'Hondt, S., Ferdelman, T.G., Ravelo, A.C., Takahashi, K., Zarijian, C.A., 2011. Coupled organic and inorganic carbon cycling in the deep subseafloor sediment of the northeastern Bering Sea Slope (IODP Exp. 323). *Chem. Geol.* 284 (3–4), 251–261.
- Willie, S.N., Sturgeon, R.E., 2001. Determination of transition and rare earth elements in seawater by flow injection inductively coupled plasma time-of-flight mass spectrometry. *Spectrochim. Acta Part B* 56, 1707–1716.